Research Square

Preprints are preliminary reports that have not undergone peer review.
They should not be considered conclusive, used to inform clinical practice,
or referenced by the media as validated information.

Bad metallicity in the semi-quantum regime of the Hubbard model

Evyatar Tulipman

tulipman@stanford.edu

Stanford University

Vadim Oganesyan

Physics Program and Initiative for the Theoretical Sciences, The Graduate Center, CUNY

Thomas Devereaux

SLAC National Accelerator Laboratory https://orcid.org/0000-0001-8072-9237

Steven Kivelson

Department of Physics https://orcid.org/0000-0001-9149-9502

Article

Keywords:

Posted Date: November 5th, 2026

DOI: https://doi.org/10.21203/rs.3.rs-11078504/v1

License: This work is licensed under a Creative Commons Attribution 4.0 International License.
Read Full License

Additional Declarations: There is **NO** Competing Interest.

Bad metallicity in the semi-quantum regime of the Hubbard model

Evyatar Tulipman,[1,2,*] Vadim Oganesyan,[3,4] Thomas P. Devereaux,[1,5,6] and Steven A. Kivelson[2]

[1] *Geballe Laboratory for Advanced Materials, Stanford University, Stanford, CA 94305, USA*

[2] *Department of Physics, Stanford University, Stanford, CA 94305, USA*

[3] *Physics Program and Initiative for the Theoretical Sciences, The Graduate Center, CUNY, New York, NY 10016, USA*

[4] *Department of Physics and Astronomy, College of Staten Island, CUNY, Staten Island, NY 10314, USA*

[5] *Stanford Institute for Materials and Energy Sciences, SLAC National Accelerator Laboratory, Menlo Park, CA 94025, USA*

[6] *Department of Materials Science and Engineering, Stanford University, Stanford, CA 94305, USA*

(Dated: October 23, 2026)

Bad metals exhibit approximately T-linear dc resistivity beyond the Ioffe–Regel limit. That this behavior occurs in systems with radically different ground states suggests it is a generic manifestation of strong local correlations. We test this hypothesis in the infinite-U Hubbard model with small hole densities using exact diagonalization to compute thermodynamic and transport properties of finite clusters. Upon cooling, we find an intermediate temperature range, an electronic analogue of the "semi-quantum regime" of liquid helium, in which quantum effects produce a roughly T-independent compressibility, yet the resistivity is T-linear and exceeds the Ioffe–Regel limit. Entry into this regime is accompanied by the formation of quasi-local ferromagnetic "spin cages" around doped holes, regions that facilitate local quantum motion embedded in a fluctuating spin background, analogous to the transient crystalline cages thought to control incoherent transport in semi-quantum liquid helium. Remarkably, despite the simplicity of the model, the bad metal behavior found here resembles that seen in various material platforms.

I. INTRODUCTION

In an ordinary metal, charge transport is dominated by electronic quasiparticles with a mean free path ℓ much longer than the Fermi wavelength λ_F. This quasiparticle picture breaks down near the Ioffe–Regel limit, $\ell \sim \lambda_F$ [1], where conventional metals often show resistivity saturation [2]. Bad metals violate this expectation: their dc resistivity, ρ, stays approximately linear

* tulipman@stanford.edu

in temperature and grows past the Ioffe–Regel scale without saturating [3–5]. Such behavior appears across strongly correlated systems from the cuprates [6] to infinite-layer nickelates [7, 8], iron-based [9] and organic conductors [10], alkali-doped fullerides [2], ruthenates [11], cold-atom Fermi–Hubbard systems [12] and possibly also magic-angle graphene [13]. While these materials exhibit extremely diverse low-temperature (T) ordering tendencies, at more elevated T they display similar bad-metallic transport, suggesting that bad metallicity is a generic finite-temperature regime of strongly correlated electrons rather than a property of any particular ordered state, quantum critical regime, or any other material-specific mechanism.

This motivates the central question: can strong local correlations alone produce bad metallicity, without invoking disorder or phonons, and if so, what is the nature of the resulting bad-metal state? Specifically, we will focus on temperatures above any ordering transition but below the electronic bandwidth.

Hubbard and Hubbard-like models have long provided the standard microscopic language for strongly correlated electronic systems [14–17]. Prior studies have shown that they can capture aspects of bad-metal phenomenology [18–30], but these studies typically focus on specific material-motivated parameters, where the existence of mesoscale ordering tendencies can obscure the origin of bad metallicity. Note that in models with a bounded single-particle spectrum, there is a well characterized "high temperature regime," $T \gg T_{\rm quant}$, where $T_{\rm quant}$ is a crossover scale proportional to the bare bandwidth, above which there is also an approximately T-linear resistivity, but one that arises from a T-independent diffusion constant, D_c, and a compressibility, $\chi_c \sim 1/T$ [28, 31, 32]. However, this high T analysis breaks down at the temperatures below the bandwidth that are relevant to the problem of bad metallicity in most realistic scenarios.

II. THE SEMI-QUANTUM REGIME

The infinite-U Hubbard model is an elegant setting in which to investigate the effects of strong local correlations: It has a single energy scale, the hopping matrix element, t; instead of an interaction there is simply the local Hilbert space constraint of no double occupancy. We study it on the two-dimensional square lattice,

$$H = -t \sum_{\langle ij \rangle, \sigma} (\tilde{c}^\dagger_{i\sigma} \tilde{c}_{j\sigma} + \text{h.c.}) \tag{1}$$

where $\tilde{c}_{i\sigma} = c_{i\sigma}(1 - n_{i\bar{\sigma}})$ and $n_{i\bar{\sigma}}$ is the electron density with spin polarization $\bar{\sigma}$ on site i. At half filling, $\langle n_{i\sigma} \rangle = 1/2$, it is a Mott insulator by construction; away from half filling it has no finite-

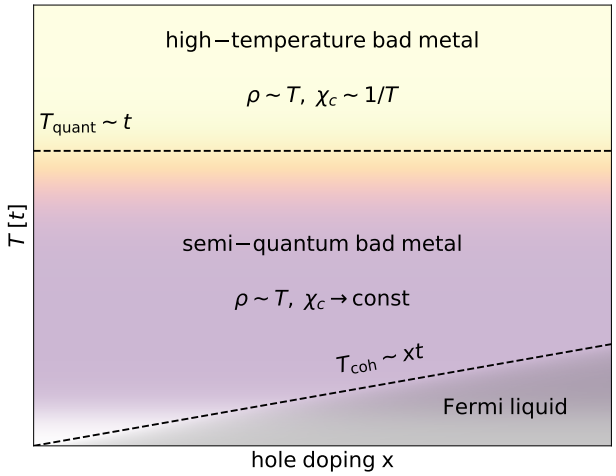


Figure 1. **Schematic transport regimes of the doped infinite-U Hubbard model.** The semi-quantum bad metal is the intermediate regime between the high-temperature bad metal, $T \gtrsim T_{\rm quant} \sim t$, and the low-temperature coherent regime, $T \lesssim T_{\rm coh} \sim xt$, where Fermi-liquid behavior is expected to emerge. Both bad-metal regimes exhibit approximately T-linear resistivity above the Ioffe–Regel scale. In the high-T regime this behavior is tied to a T-dependent compressibility, $\chi_c \sim 1/T$, whereas in the semi-quantum regime χ_c departs from this form and approaches a constant, signaling the onset of quantum dynamics, even as charge transport remains incoherent. Dashed lines indicate crossovers, not sharp phase boundaries.

temperature ordered phase. The model exhibits an emergent low-energy coherence scale, $T_{\rm coh}$, which in the limit of small hole concentration, $x \ll 1$, is parametrically small, $T_{\rm coh} \sim xt \ll T_{\rm quant}$. More concretely, the ground state is ferromagnetic for a single hole [33] and was demonstrated numerically to remain so up to hole-doping $x \lesssim 0.2$ in two dimensions [34], with a spin-stiffness scale $\rho_s \sim xt$ at $T = 0$. Thus, $T_{\rm coh} \sim xt$ can be taken to be the temperature below which the ferromagnetic correlation length begins to grow exponentially (i.e. $\xi \sim e^{2\pi\rho_s/T}$) with decreasing T (App. G).

Here, we characterize the intermediate regime $T_{\rm quant} \gtrsim T \gtrsim T_{\rm coh}$, schematically shown in Fig. 1, where $T_{\rm quant} \sim t$ marks the onset of quantum dynamics and $T_{\rm coh} \sim xt$ the scale at which coherent charge motion onsets. Using exact diagonalization, we obtain the full many-body spectrum and all current matrix elements, enabling numerically exact calculations of thermodynamics and transport on 4×4, $\sqrt{18} \times \sqrt{18}$, and 4×5 clusters. We find that, upon cooling from above $T_{\rm quant}$, where the resistivity is already T-linear but the compressibility $\sim 1/T$, the system enters a regime in which thermodynamic quantities such as the compressibility reflect the quantum dynamics, yet the resistivity remains above the Ioffe–Regel limit and approximately T-linear, albeit with a different slope than at high-T. The essential hierarchy, $T_{\rm quant} \gg T_{\rm coh}$, has no analogue in a weakly correlated

metal.

Such a separation between the scales is the defining feature of the "semi-quantum liquid" introduced by Andreev and Kosevich [35, 36] in the context of liquid He. Their key physical insight was that in a range of T, quantum effects are manifest when the level spacings associated with the motion of a single particle in a local "cage" are larger than T, while coherent exchange processes that are consequences of quantum statistics are only significant at much lower T. They further argued that this regime exhibits a viscosity (and hence a diffusion constant) proportional to $1/T$. In the present case, the local cage is not produced by positional correlations, as in liquid helium, but by the fluctuating spin background through which a doped hole moves. As we show below, the hole develops a finite ferromagnetic environment in which its motion is less kinetically frustrated. This polarized region acts as a self-generated "spin cage" that permits quantum motion locally while inhibiting coherent propagation over longer distances; it appears near $T_{\rm quant}$ and expands in radius only near $T_{\rm coh}$, providing a real-space manifestation of the separation between local quantum dynamics and global quantum coherence that defines the semi-quantum regime. Generalizing from these observations, we conjecture that local caging and an approximately T-linear inverse diffusivity may be general features of semi-quantum liquids in more realistic models of strongly interacting electrons (possibly including interactions with phonons), even though the microscopic nature of the cages surely differs from case to case.

III. SEMI-QUANTUM BAD-METAL TRANSPORT

Figure 2 presents the central result. The dc resistivity is approximately T-linear and lies above the Ioffe–Regel limit across the temperature window $T_{\rm coh} \lesssim T \leq t$ (i.e. ending somewhere in the crossover regime between the semi-quantum and high temperature behavior) for dopings $x = 1/20$, $1/18$, $1/16$, and $2/16$ (Fig. 2A). We take the Ioffe–Regel scale of a two-dimensional metal to be $\rho_{\rm IR} = \hbar/e^2$, corresponding to $k_F\ell \sim 2\pi$ (horizontal dashed line in Fig. 2A). Dashed lines in Fig. 2A are T-linear fits to ρ in the semi-quantum regime; the inset highlights the distinct T-linear slopes in the high-T and semi-quantum regimes, shown over a wider range of temperatures. The T-linearity in the two regimes have physically distinct origins, revealed by the Nernst–Einstein relation $\rho = 1/(\chi_c D_c)$, which expresses the resistivity as the product of a thermodynamic factor, the compressibility χ_c, and a dynamical factor, the charge diffusivity D_c (Fig. 2B,C). At high temperatures, the inverse compressibility $1/\chi_c$ rises approximately linearly with T, as expected from the high-temperature expansion (dashed curve, Fig. 2B; see also App. F); in this regime

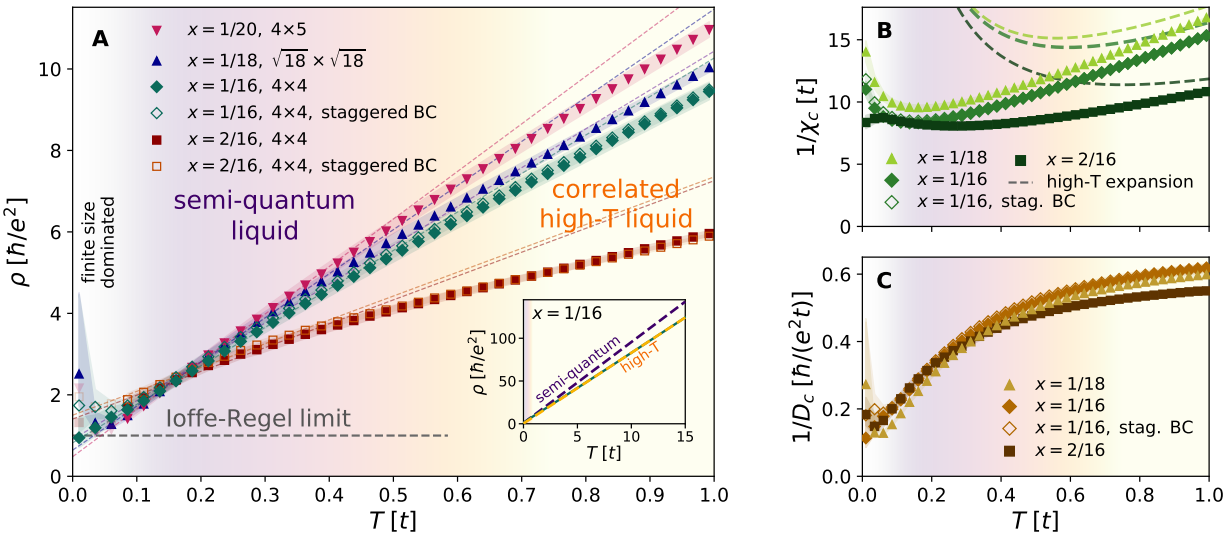


Figure 2. **Bad-metallic transport regimes.** (A) Twist-averaged dc resistivity for $x = 1/20$, $1/18$, $1/16$, and $2/16$. The resistivity is approximately T-linear and above the Ioffe–Regel scale, but with a slope change near $T_{\rm quant}$: the dashed lines are linear fits to the data in the semi-quantum regime. The inset compares linear fits to $\rho(T)$ in the high-T and semi-quantum regimes over an expanded range of T. Results are shown for non-staggered and staggered boundary conditions. (B,C) Nernst–Einstein decomposition, $\rho = 1/(\chi_c D_c)$. The dashed curve in (B) is the first-order high-temperature expansion. Shaded bands indicate the standard deviation over different twisted boundary conditions.

the T-linear resistivity is largely thermodynamic in origin. Below $T_{\rm quant} \approx 0.5$–$0.8t$, identified operationally by the departure of $1/\chi_c$ from the high-temperature form, the inverse compressibility saturates toward a nearly constant value, signaling the importance of quantum dynamics. The dominant temperature dependence of ρ has shifted from thermodynamics to dynamics: it is now carried by the inverse diffusivity $1/D_c$, which becomes approximately T-linear in the semi-quantum regime (Fig. 2C). This is the key observation: Below $T_{\rm quant}$, bad metallicity is no longer the high-temperature thermodynamic contribution extended downward; instead it is a property of incoherent charge quantum dynamics, encoded in the diffusivity D_c.

The explicit calculations we have carried out are on clusters with toroidal geometries. As one way of assessing finite-size effects, we compare results for different periodic cluster connectivities (distinct Betts cluster geometries [37]), which we refer to as "staggered" and "non-staggered" and illustrate in Fig. 6 of App. A. Moreover, to reduce finite-size effects, for each cluster geometry, we apply boundary conditions corresponding to phase "twists" $\Delta\theta_a$, $a = x, y$, in the two orthogonal directions around the torus (which can be thought of as corresponding to fractions of a flux quantum through the holes of the torus), where unless otherwise stated, calculations are carried out for 25

values of $\Delta\theta_a = 2\pi\,(n_a + \varphi)\,/5$ with $0 \le n_a < 5$ and an irrational offset $\varphi = (1+\sqrt{5})/2$. As is illustrated in Fig. 2, the differences in the results for the staggered and unstaggered geometries and the twist variance of the results are small for $T \gtrsim 0.08t$. This weak sensitivity to cluster geometry is also consistent with transport being controlled primarily by short-range correlations. At lower temperatures, the twist variance grows and the two geometric sectors separate, marking the onset of a finite-size-dominated regime at T near $T_{\rm coh}$. Fortunately, the accessible T window in which finite-size effects are plausibly negligible includes the relevant semi-quantum regime.

IV. OPTICAL AND THERMODYNAMIC SIGNATURES

The optical conductivity reveals how charge dynamics evolve across the crossover into the semi-quantum regime (Fig. 3, A–D; shaded bands show the twist variance). At high temperatures, $\sigma(\omega, T)$ is broad and nearly featureless, consistent with incoherent charge motion. Upon cooling below $T_{\rm quant}$, low-frequency spectral weight builds up into an enhanced peak at low frequencies. The response, however, remains broad – on the scale of t; it is an incipient Drude-like feature but not a sharp quasiparticle peak. Over the same temperature range, the one-hole optical spectra also develop a broad finite-frequency feature at frequencies of order t, rather than a clean separation into a narrow Drude peak and a high-energy background.

The low-frequency insets show a slight downturn as $\omega \to 0$, which we attribute to finite-cluster artifacts [31]. We obtain $\sigma_{\rm dc}$ from the quadratic low-frequency extrapolation illustrated in the insets; varying the fitting window and functional form changes $\sigma_{\rm dc}$ by less than a few percent for $T \gtrsim 0.08t$, comparable to the twist standard deviation. Details are given in App. C 2.

We quantify the buildup and narrowing of the low-frequency response as follows: We define a "coherence ratio," $R_{\rm coh}(T) = \sigma_{\rm dc}(T)/\sigma(\omega = 0.5t, T)$. As shown in Fig. 3E, $R_{\rm coh}$ begins to grow near $T_{\rm quant}$, providing an optical signature of the crossover into the semi-quantum regime. A sharply coherent Drude response would give $R_{\rm coh} \gg 1$, whereas throughout most of the semi-quantum regime it remains $\mathcal{O}(1)$, consistent with a broad low-frequency response rather than a coherent Drude peak. To characterize the narrowing of the low-frequency feature without assuming a specific functional form, we define the change in optical conductivity relative to a fixed high-temperature reference, $\Delta\sigma(\omega, T) = \sigma(\omega, T) - \sigma(\omega, T_{\rm ref})$, with $T_{\rm ref} = t$. We characterize the frequency extent of the low-frequency feature by its high-frequency half-maximum edge, $\Delta\omega(T)$, defined by $\Delta\sigma(\Delta\omega, T) = \frac{1}{2}\Delta\sigma_{\rm dc}(T)$, with $\Delta\omega > \omega_{\rm max}$, where $\omega_{\rm max}$ denotes the position of the maximum of $\Delta\sigma(\omega, T)$. As shown in Fig. 3F, $\Delta\omega$ decreases approximately linearly upon cooling for the one-hole

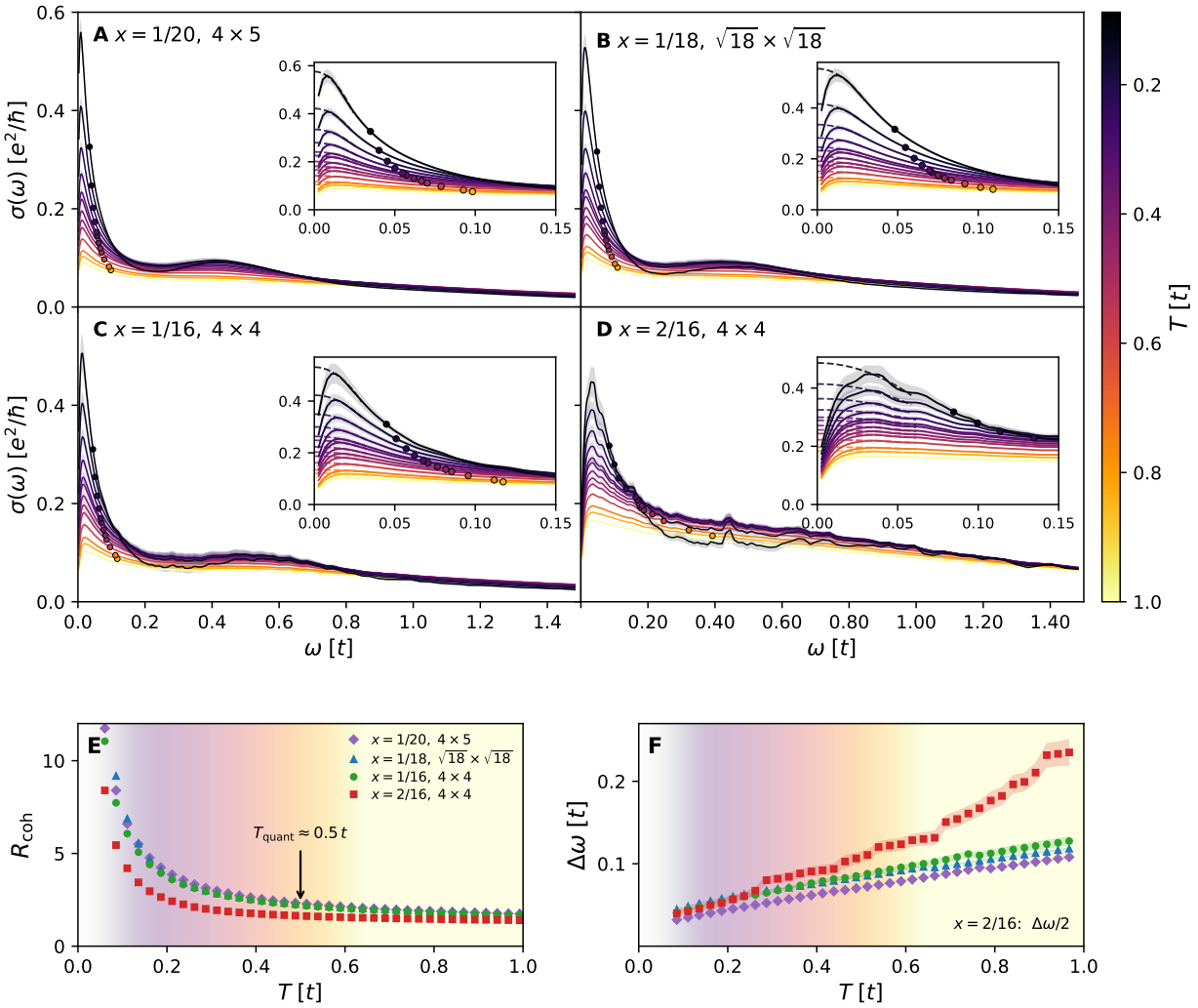


Figure 3. **Optical conductivity in the semi-quantum regime.** (**A**–**D**) optical conductivity $\sigma(\omega, T)$ for $x = 1/20$ (**A**; 4×5), $x = 1/18$ (**B**; $\sqrt{18} \times \sqrt{18}$), and $x = 1/16$, $2/16$ (**C, D**; 4×4), with curves colored by temperature. Shaded bands indicate the standard error over boundary twists; insets show the low-frequency extrapolation used to obtain σ_{dc}. The low frequency portion of σ can be characterized by (**E**) a weight, $R_{\mathrm{coh}} = \sigma_{\mathrm{dc}}/\sigma(\omega = 0.5t)$, and (**F**) a width, $\Delta\omega(T)$, defined by $\Delta\sigma(\Delta\omega, T) = \frac{1}{2}\Delta\sigma_{\mathrm{dc}}(T)$, with $\Delta\omega > \omega_{\mathrm{max}}$, ω_{max} being the position of the maximum of $\Delta\sigma(\omega, T)$. The $x = 2/16$ values in (**F**) are multiplied by $1/2$ for visual comparison. (Values of σ at $\Delta\omega(T)$ are also indicated by the filled circles in A–D.)

clusters, demonstrating the progressive narrowing of the low-frequency feature. (The filled circles in (A–D) mark $\sigma(\omega, T)$ at $\omega = \Delta\omega(T)$.) Note that the two-hole results are qualitatively distinct, with a larger characteristic frequency scale and a different temperature dependence. With the system sizes presently accessible, we cannot determine whether these differences reflect the higher doping or finite-size effects. For visual comparison, the $x = 2/16$ values in Fig. 3F are multiplied by $1/2$.

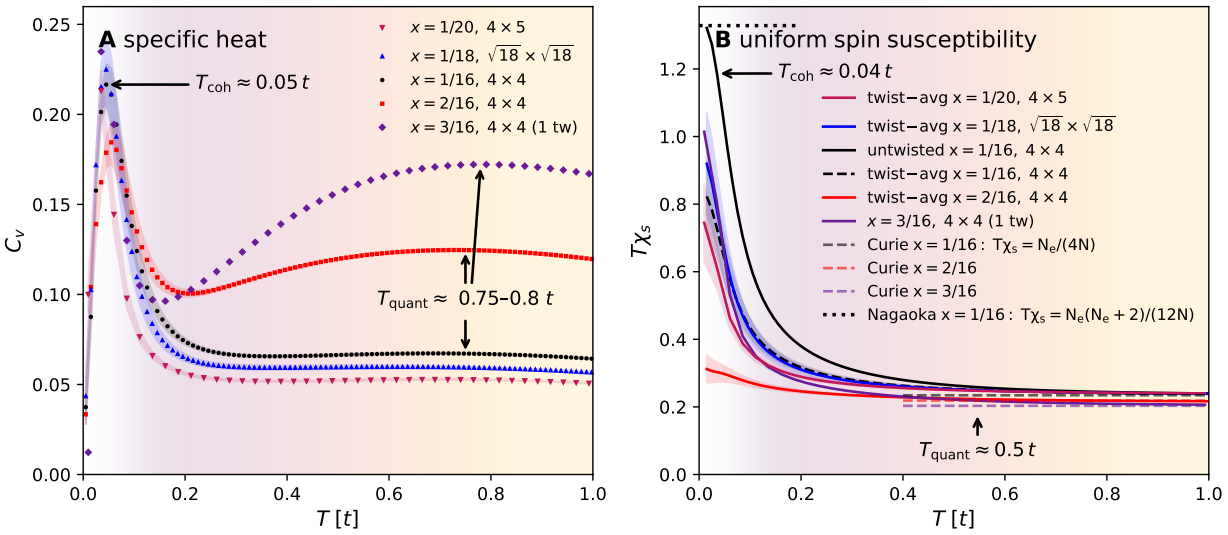


Figure 4. **Thermodynamics across the semi-quantum crossover.** (**A**) Specific heat per site for $x = 1/20, 1/18, 1/16, 2/16$, and $3/16$. (**B**) Uniform spin susceptibility for the indicated dopings and boundary conditions; dashed lines show the Curie and finite-cluster Nagaoka values. Shaded bands indicate the standard error over boundary twists. Data for $x = 3/16$ are shown for a single irrational twist.

Changing the reference temperature shifts the absolute values of $\Delta\omega$ somewhat, particularly at low temperature, but leaves the qualitative temperature dependence unchanged (see App. C 4).

The specific heat and uniform spin susceptibility provide complementary thermodynamic signatures of the semi-quantum crossover (Fig. 4). In panel A, C_V develops a broad maximum near $T_{\rm quant} \approx 0.75t$, marking its departure from the classical high-temperature behavior $C_V \sim 1/T^2$, followed by a much sharper peak near the lower scale $T_{\rm coh}$ associated with the approach to the spin-polarized ferromagnetic ground state. Panel B shows $\chi_s = (\langle S_z^2\rangle - \langle S_z\rangle^2)/(NT)$ for $x = 1/18$, $1/16$, and $2/16$. All dopings depart near $T_{\rm quant}$ from the independent-moment Curie form, $\chi_s = (1-x)/(4T)$. For the untwisted single-hole 4×4 cluster, χ_s approaches the finite-cluster Nagaoka value, $\chi_s^{\rm Nag} = N_e(N_e+2)/(12NT)$, only at much lower temperature [38]. We define $T_{\rm coh}$ operationally as the temperature at which the untwisted susceptibility lies within 10% of $\chi_s^{\rm Nag}$, consistent with $T_{\rm coh} \sim xt$. Together with the charge compressibility, the specific heat and spin susceptibility show that the semi-quantum crossover occurs near the same scale across the charge, spin, and energy sectors.

V. FORMATION OF A SPIN CAGE

The Andreev–Kosevich picture suggests a concrete real-space criterion for the electronic semiquantum regime. At $T_{\rm quant}$, the onset of quantum dynamics should be accompanied with the existence of a finite local "cage" in which there are well-separated discrete quantum states of an individual carrier, but this environment should remain spatially bounded until coherent motion emerges near $T_{\rm coh}$. In the infinite-U Hubbard model, the cage is provided not by positional correlations but by the fluctuating spin background through which the doped hole moves. Successive hole hops permute the spins along its path, so motion through a disordered background continually rearranges the spin configuration [39]. Local ferromagnetic correlations reduce the kinetic frustration, allowing the hole to move more effectively within a polarized region. At finite temperature, however, the kinetic-energy gain competes with the entropic cost of polarizing an extended region. The result is a finite ferromagnetic environment within which hole motion is coherent, but beyond which it again encounters a disordered and kinetically frustrating spin background. It is in this sense that the polarized region constitutes a cage.

We probe this structure directly using the connected hole–spin-bond correlator

$$C_h(\mathbf{R},\mathbf{e};T) = \left\langle \rho_h(\mathbf{0})\, \mathbf{S}_{\mathbf{R}-\mathbf{e}/2}\cdot\mathbf{S}_{\mathbf{R}+\mathbf{e}/2}\right\rangle_T - \langle\rho_h(\mathbf{0})\rangle_T \left\langle \mathbf{S}_{\mathbf{R}-\mathbf{e}/2}\cdot\mathbf{S}_{\mathbf{R}+\mathbf{e}/2}\right\rangle_T . \tag{2}$$

Here, $\rho_h(\mathbf{0})$ is the hole density at the origin, $\mathbf{R}$ is the displacement from the hole to the center of a nearest-neighbor bond oriented in the $\mathbf{e} = \hat{\mathbf{x}}, \hat{\mathbf{y}}$ direction. Thus, C_h is the change in the local spin correlations induced by the presence of a nearby hole.

Figure 5A shows the radial profile $C_h(R,T)$ of the hole-induced spin correlations, extracted from $C_h(\mathbf{R},\mathbf{e};T)$ using bond centers that lie a distance $R = |\mathbf{R}|$ from the hole, normalized by the value in the Nagaoka ferromagnetic ground state $x^2/2$ (App. E). The results are evaluated for an untwisted boundary on the 18-site cluster; Fig. 5B shows the corresponding bond-resolved textures. As T is lowered from above to below $T_{\rm quant}$, the hole gradually polarizes its immediate surroundings, while the more distant spin background remains weakly affected. The resulting finite-radius ferromagnetic texture defines the *spin cage*. Only upon cooling below $T_{\rm coh}$ does the ferromagnetic correlation length grow beyond the cluster size, marking the crossover to coherent (Fermi liquid) charge motion and the approach to the $T = 0$ ferromagnetic ground state.

The formation of a finite polarized region around the hole, embedded in an otherwise fluctuating spin background, suggests that the hole motion may be effectively restricted to this spin cage. To test this, we construct a trial system in which the hole is confined to a subregion comparable in

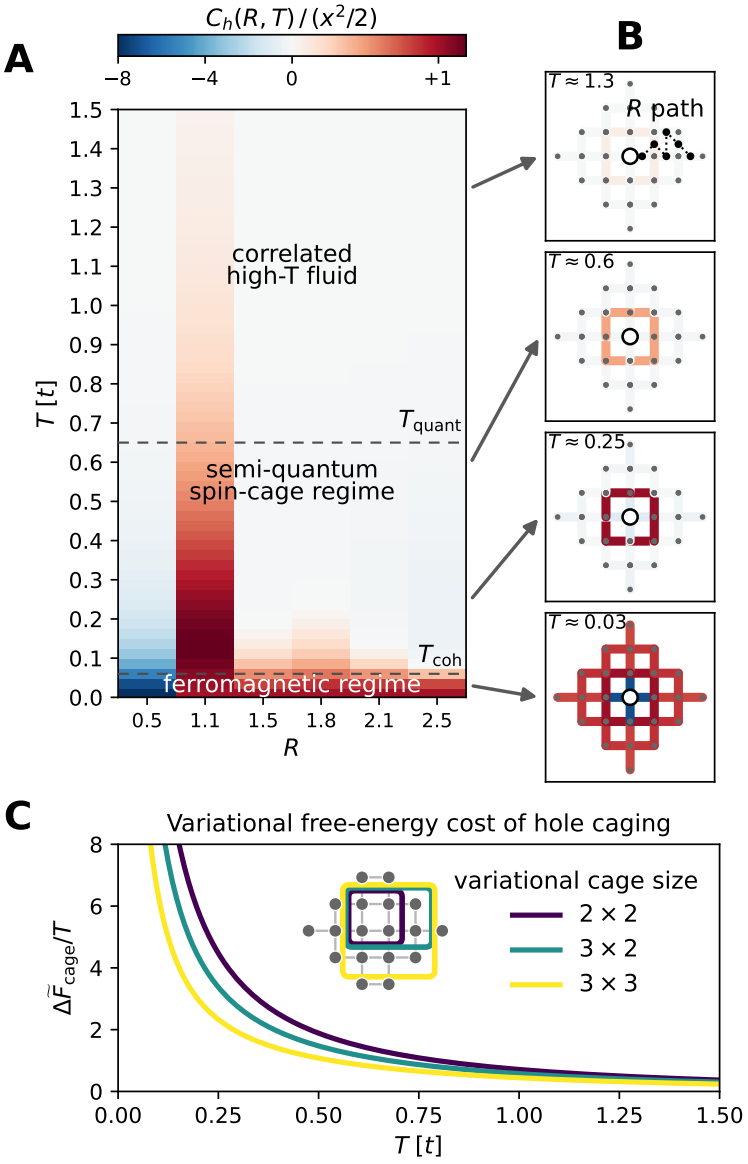


Figure 5. **Formation and variational cost of a spin cage. A**, Connected hole–spin-bond correlator $C_h(R,T)$ for a representative boundary twist on the 18-site cluster, normalized by $x^2/2$, the value of C_h in the Nagaoka ground state. **B**, Corresponding bond-resolved patterns of $C_h(\mathbf{R},\mathbf{e};T)$ at selected temperatures; the path used to define R in panel (**A**) is indicated in the top panel of (**B**). **C**, Variational free-energy cost $\Delta\widetilde{F}_{\rm cage}/T$ of restricting the hole to the indicated finite regions as a function of T.

size to the spin texture while the exterior remains half filled, and compute the corresponding free energy $F_{\rm tr}$, which provides a variational upper bound on the full free energy F (App. H). At high temperatures, $\Delta F_{\rm cage} \equiv F_{\rm tr} - F$ approaches $T\ln(N/N_{\rm cage})$, the free-energy cost associated with the loss of positional entropy upon restricting the hole to $N_{\rm cage}$ of the N sites. We therefore consider $\Delta\widetilde{F}_{\rm cage} \equiv \Delta F_{\rm cage} - T\ln(N/N_{\rm cage})$, the confinement cost beyond this positional contribution. As

shown in Fig. 5C, at high temperatures this residual cost is small, consistent with the approximate locality of the free energy. Around $T_{\rm quant}$ we find $\Delta\widetilde{F}_{\rm cage} \sim T$, and $\Delta\widetilde{F}_{\rm cage}/T$ remains of order unity through much of the semi-quantum regime. Thus, although the free energy is no longer strictly local, confinement on the scale of the spin texture costs of order the thermal scale, consistent with a fluctuating rather than static cage. On approaching $T_{\rm coh}$, $\Delta\widetilde{F}_{\rm cage}/T$ grows rapidly, signaling the breakdown of this local confinement description as ferromagnetic correlations spread across the system.

VI. DISCUSSION AND OUTLOOK

Our discussion thus far has largely treated the calculations as a numerical experiment, focusing on the essential features of the semi-quantum regime with minimal interpretation. Most observables are consistent with a dilute, yet strongly correlated limit, with relatively small subleading corrections in x. The two-hole transport results show larger deviations, including a broader low-frequency optical response, although with the system sizes presently accessible we cannot distinguish genuine doping dependence from finite-size effects. A more puzzling feature revealed by our results is the behavior of the compressibility in the semi-quantum regime: it becomes approximately independent of both T and x, yet remains about 1.5 times larger than the $T = 0$ Nagaoka value of the spin-polarized Fermi liquid, $\chi_c = 1/(4\pi t)$, approaching that value only at much lower temperatures near $T_{\rm coh}$. Thus, the nearly T-independent quantum response that develops below $T_{\rm quant}$ remains distinct from the eventual low-temperature quasiparticle regime. A natural starting point for a theory of the semi-quantum regime may be the dynamics of a single caged hole, with some similarity to local descriptions underlying DMFT studies of bad metallicity. However, as shown in App. D, vertex corrections must be retained for quantitative transport: comparing the full Kubo result with the bubble conductivity constructed from the same exact spectral function isolates a sizable vertex contribution, as also suggested by related comparisons of the finite-U Hubbard model [12, 40]. The short-ranged correlations nevertheless suggest that a tractable quasi-local description may be possible.

We now comment on what we see as the physical relevance of our results to the properties of strongly correlated metals. The central significance of our results lies neither in the conventional low-temperature coherent regime nor in the asymptotic high-temperature limit, but in the intermediate regime separating them. The low T behavior has much in common with behavior of many materials in that it can be understood in terms of broken symmetries and well-defined

quasi-particles. The high T behavior is probably not relevant to typical quantum materials, since it derives from the boundedness of the spectrum of the tight -binding model - although it may be relevant in certain "flat band" contexts. Our key finding is that - rather than a smooth crossover between these two extremal regimes - there is a well-defined intermediate semi-quantum regime in which the particles are largely confined in relatively small emergent cages. The microscopic origin of the T-linear inverse diffusivity remains to be understood. Nevertheless, the resistivity in this regime is roughly $T-$linear, as in the high T regime but with a different slope and extrapolated intercept, while thermodynamic quantities, such as the compressibility, exhibit a T dependence similar to that in the low T regime, albeit with different magnitudes. The physics driving this is local - and indeed it likely does not depend in any significant way on the quantum statistics of the particles.

Cold-atom systems are particularly promising for testing this picture because local correlations can in principle be imaged directly and related to transport in the same controlled setting. Local dopant–spin correlations closely related to the spin cages identified here have already been resolved in Fermi–Hubbard quantum simulators [41–45], while bad-metal transport and charge diffusion have been measured in cold-atom Hubbard systems [12, 46]. Such platforms therefore offer the prospect of tracking the temperature evolution of local caging alongside charge diffusion, directly testing their interplay in the semi-quantum regime. Moreover, if the essential physics is independent of particle statistics, analogous behavior may also be accessible in strongly interacting bosonic systems, broadening the range of platforms in which this physics can be explored.

We conclude by speculating that the bad-metal regimes of a broader class of correlated electronic systems may reflect analogous semi-quantum physics. The nature of the "cages" will naturally vary greatly from case to case - it can be local nearly crystalline environments as in liquid He (and possibly in the 2D electron fluid at large r_s [47]) or a polaronic distortion in the case of strong electron-phonon coupling, or can even be largely structural in character, as for example in a C_{60} molecule in A_3C_{60} [48, 49]. It is at least intuitively clear how such local fluctuating cage structures can lead to long incoherent tails in the optical conductivity. What remains less clear is why, and under what general conditions, they produce both the buildup of low-frequency spectral weight and T-linear resistivity. The present results suggest that a theory of this kind may be possible using only the physics of strong local correlations.

ACKNOWLEDGMENTS

SAK particularly thanks B. Spivak for his obsession with the semiquantum fluid over many years. We also acknowledge significant discussions with Srinivas Raghu, Noga Bashan, Erez Berg, Pavel Nosov, Antoine Georges, Andrey Chubukov and Lev Ioffe. ET thanks Guy Tevet for a useful discussion on GPU-based diagonalization. ChatGPT (OpenAI) and Claude (Anthropic) were used as technical aids for code optimization and debugging, preparation of plotting scripts, and manuscript editing. All scientific methodology, numerical results, analysis, and interpretation were developed and validated by the authors. ET was supported in part by NSF-BSF award DMR-2310312, a research gift from Periodic Labs, Inc.,the Zuckerman STEM fellowship and the Geballe Laboratory of Advanced Materials Postdoctoral Fellowship, TPD and SAK were supported by the U.S. Department of Energy (DOE), Office of Science, Basic Energy Sciences, Materials Sciences and Engineering Division, under contract DE-AC02-76SF00515. Computational work was performed on the Sherlock cluster at Stanford University and on resources of the National Energy Research Scientific Computing Center, supported by the U.S. Department of Energy under award BES-ERCAP0034969.

---

[1] A. F. Ioffe and A. R. Regel, Non-crystalline, amorphous and liquid electronic semiconductors, Progress in Semiconductors **4**, 237 (1960).

[2] O. Gunnarsson, M. Calandra, and J. E. Han, Colloquium: Saturation of electrical resistivity, Reviews of Modern Physics **75**, 1085 (2003).

[3] V. J. Emery and S. A. Kivelson, Superconductivity in bad metals, Physical Review Letters **74**, 3253 (1995).

[4] N. E. Hussey, K. Takenaka, and H. Takagi, Universality of the mott–ioffe–regel limit in metals, Philosophical Magazine **84**, 2847 (2004).

[5] P. W. Phillips, N. E. Hussey, and P. Abbamonte, Stranger than metals, Science **377**, eabh4273 (2022).

[6] B. Keimer, S. A. Kivelson, M. R. Norman, S. Uchida, and J. Zaanen, From quantum matter to high-temperature superconductivity in copper oxides, Nature **518**, 179 (2015).

[7] K. Lee, B. Y. Wang, M. Osada, B. H. Goodge, T. C. Wang, Y. Lee, S. P. Harvey, W. J. Kim, Y. Yu, C. Murthy, S. Raghu, L. F. Kourkoutis, and H. Y. Hwang, Linear-in-temperature resistivity for optimally superconducting (Nd,Sr)NiO_2, Nature **619**, 288 (2023).

[8] Y.-T. Hsu, K. Lee, S. Badoux, C. Duffy, A. Cuoghi, B. Y. Wang, A. Kool, I. Haïk-Dunn, H. Y. Hwang, and N. E. Hussey, Transport phase diagram and anomalous metallicity in superconducting infinite-layer nickelates, Nature Communications **15**, 9863 (2024).

[9] S. Kasahara, T. Shibauchi, K. Hashimoto, K. Ikada, S. Tonegawa, R. Okazaki, H. Shishido, H. Ikeda, H. Takeya, K. Hirata, T. Terashima, and Y. Matsuda, Evolution from non-fermi- to fermi-liquid transport via isovalent doping in $BaFe_2(As_{1-x}P_x)_2$ superconductors, Physical Review B **81**, 184519 (2010).

[10] A. N. Bloch, D. O. Cowan, and T. O. Poehler, Organic conductors ii: TTF–TCNQ and other organic semimetals, in *Energy and Charge Transfer in Organic Semiconductors*, edited by K. Masuda and M. Silver (Plenum Press, New York, 1974) pp. 167–174.

[11] A. W. Tyler, A. P. Mackenzie, S. NishiZaki, and Y. Maeno, High-temperature resistivity of Sr_2RuO_4: Bad metallic transport in a good metal, Physical Review B **58**, R10107 (1998).

[12] P. T. Brown, D. Mitra, E. Guardado-Sanchez, R. Nourafkan, A. Reymbaut, C.-D. Hébert, S. Bergeron, A.-M. S. Tremblay, J. Kokalj, D. A. Huse, P. Schauss, and W. S. Bakr, Bad metallic transport in a cold atom Fermi–Hubbard system, Science **363**, 379 (2019).

[13] Y. Cao, D. Chowdhury, D. Rodan-Legrain, O. Rubies-Bigorda, K. Watanabe, T. Taniguchi, T. Senthil, and P. Jarillo-Herrero, Strange metal in magic-angle graphene with near Planckian dissipation, Physical Review Letters **124**, 076801 (2020).

[14] D. P. Arovas, E. Berg, S. A. Kivelson, and S. Raghu, The hubbard model, Annual Review of Condensed Matter Physics **13**, 239 (2022), arXiv:2103.12097 [cond-mat.str-el].

[15] E. Dagotto, Correlated electrons in high-temperature superconductors, Reviews of Modern Physics **66**, 763 (1994), arXiv:cond-mat/9311013.

[16] P. A. Lee, N. Nagaosa, and X.-G. Wen, Doping a Mott insulator: Physics of high-temperature superconductivity, Reviews of Modern Physics **78**, 17 (2006).

[17] M. Qin, T. Sch"afer, S. Andergassen, P. Corboz, and E. Gull, The hubbard model: A computational perspective, Annual Review of Condensed Matter Physics **13**, 275 (2022), arXiv:2104.00064 [cond-mat.str-el].

[18] J. Jaklič and P. Prelovšek, Finite-temperature conductivity in the planar t-J model, Physical Review B **50**, 7129 (1994).

[19] J. Jaklič and P. Prelovšek, Charge dynamics in the planar t-J model, Physical Review B **52**, 6903 (1995).

[20] M. M. Zemljič and P. Prelovšek, Resistivity and optical conductivity of cuprates within the t-J model, Physical Review B **72**, 075108 (2005).

[21] E. W. Huang, R. Sheppard, B. Moritz, and T. P. Devereaux, Strange metallicity in the doped Hubbard model, Science **366**, 987 (2019).

[22] S. Zhao, R. Zhang, W. O. Wang, J. K. Ding, T. Liu, B. Moritz, E. W. Huang, and T. P. Devereaux, Enhanced superconducting correlations in the Emery model and its connections to strange metallic transport and normal state coherence, Physical Review B **112**, 224513 (2025).

[23] X. Deng, J. Mravlje, R. Žitko, M. Ferrero, G. Kotliar, and A. Georges, How bad metals turn good: Spectroscopic signatures of resilient quasiparticles, Physical Review Letters **110**, 086401 (2013).

[24] J. Merino and R. H. McKenzie, Transport properties of strongly correlated metals: A dynamical mean-

field approach, Physical Review B **61**, 7996 (2000).

[25] J. Vučičević, D. Tanasković, M. J. Rozenberg, and V. Dobrosavljević, Bad-metal behavior reveals Mott quantum criticality in doped Hubbard models, Physical Review Letters **114**, 246402 (2015).

[26] A. Vranić, J. Vučičević, J. Kokalj, and R. Žitko, Charge transport in the Hubbard model at high temperatures, Physical Review B **102**, 115142 (2020).

[27] J. Jaklič and P. Prelovšek, Finite-temperature properties of doped antiferromagnets, Advances in Physics **49**, 1 (2000).

[28] J. Kokalj, Bad-metallic behavior of doped mott insulators, Physical Review B **95**, 041110 (2017).

[29] N. H. Lindner and A. Auerbach, Conductivity of hard core bosons: A paradigm of a bad metal, Physical Review B **81**, 054512 (2010).

[30] S. Liu, Y. Ma, H. J. Changlani, P. W. Phillips, and B. A. Bernevig, Transport and temperature 1: Exact spectrum and resistivity for the one-dimensional infinite-U Hubbard model (2026), arXiv:2604.02426 [cond-mat.str-el].

[31] S. Mukerjee, V. Oganesyan, and D. Huse, Statistical theory of transport by strongly interacting lattice fermions, Physical Review B **73**, 035113 (2006).

[32] E. Perepelitsky, A. Galatas, J. Mravlje, R. Žitko, E. Khatami, B. S. Shastry, and A. Georges, Transport and optical conductivity in the hubbard model: A high-temperature expansion perspective, Physical Review B **94**, 235115 (2016).

[33] Y. Nagaoka, Ferromagnetism in a narrow, almost half-filled s band, Physical Review **147**, 392 (1966).

[34] L. Liu, H. Yao, E. Berg, S. R. White, and S. A. Kivelson, Phases of the infinite U Hubbard model on square lattices, Physical Review Letters **108**, 126406 (2012).

[35] A. F. Andreev, Thermodynamics of liquids below the Debye temperature, JETP Letters **28**, 556 (1978), pis'ma Zh. Eksp. Teor. Fiz. 28, 603 (1978).

[36] A. F. Andreev and Y. A. Kosevich, Kinetic phenomena in semiquantum liquids, Soviet Physics JETP **50**, 1218 (1979), zh. Eksp. Teor. Fiz. 77, 2518 (1979).

[37] D. D. Betts, H. Q. Lin, and J. S. Flynn, Improved finite-lattice estimates of the properties of two quantum spin models on the infinite square lattice, Canadian Journal of Physics **77**, 353 (1999).

[38] J. A. Riera and A. P. Young, Ferromagnetism in the one-band Hubbard model, Physical Review B **40**, 5285 (1989).

[39] W. F. Brinkman and T. M. Rice, Single-particle excitations in magnetic insulators, Physical Review B **2**, 1324 (1970).

[40] J. Vučičević, J. Kokalj, R. Žitko, N. Wentzell, D. Tanasković, and J. Mravlje, Conductivity in the square lattice hubbard model at high temperatures: Importance of vertex corrections, Physical Review Letters **123**, 036601 (2019).

[41] J. Koepsell, J. Vijayan, P. Sompet, F. Grusdt, T. A. Hilker, E. Demler, G. Salomon, I. Bloch, and C. Gross, Imaging magnetic polarons in the doped fermi–hubbard model, Nature **572**, 358 (2019).

[42] G. Ji, M. Xu, L. H. Kendrick, C. S. Chiu, J. C. Brüggenjürgen, D. Greif, A. Bohrdt, F. Grusdt,

E. Demler, M. Lebrat, and M. Greiner, Coupling a mobile hole to an antiferromagnetic spin background: Transient dynamics of a magnetic polaron, Phys. Rev. X **11**, 021022 (2021).

[43] J. Koepsell, D. Bourgund, P. Sompet, S. Hirthe, A. Bohrdt, Y. Wang, F. Grusdt, E. Demler, G. Salomon, C. Gross, and I. Bloch, Microscopic evolution of doped Mott insulators from polaronic metal to Fermi liquid, Science **374**, 82 (2021).

[44] M. Lebrat, M. Xu, L. H. Kendrick, A. Kale, Y. Gang, P. Seetharaman, I. Morera, E. Khatami, E. Demler, and M. Greiner, Observation of Nagaoka polarons in a Fermi–Hubbard quantum simulator, Nature **629**, 317 (2024).

[45] M. L. Prichard, B. M. Spar, I. Morera, E. Demler, Z. Z. Yan, and W. S. Bakr, Directly imaging spin polarons in a kinetically frustrated Hubbard system, Nature **629**, 323 (2024).

[46] W. Xu, W. R. McGehee, W. N. Morong, and B. DeMarco, Bad-metal relaxation dynamics in a Fermi lattice gas, Nature Communications **10**, 1588 (2019).

[47] B. Spivak, S. V. Kravchenko, S. A. Kivelson, and X. P. A. Gao, Colloquium: Transport in strongly correlated two dimensional electron fluids, Rev. Mod. Phys. **82**, 1743 (2010).

[48] A. F. Hebard, T. T. M. Palstra, R. C. Haddon, and R. M. Fleming, Absence of saturation in the normal-state resistivity of thin films of K_3C_{60} and Rb_3C_{60}, Phys. Rev. B **48**, 9945 (1993).

[49] O. Gunnarsson, Superconductivity in fullerides, Rev. Mod. Phys. **69**, 575 (1997).

[50] NVIDIA Corporation, *cuSOLVERMp: A High-Performance CUDA Library for Distributed Dense Linear Algebra*, NVIDIA Corporation, version 0.8.0 (CUDA 12), accessed August 1, 2026.

[51] W. Kohn, Theory of the insulating state, Physical Review **133**, A171 (1964).

[52] D. Poilblanc, Twisted boundary conditions in cluster calculations of the optical conductivity in two-dimensional lattice models, Physical Review B **44**, 9562 (1991).

[53] X. Zotos, F. Naef, and P. Prelovšek, Transport and conservation laws, Phys. Rev. B **55**, 11029 (1997).

[54] R. E. Prange and L. P. Kadanoff, Transport Theory for Electron-Phonon Interactions in Metals, Physical Review **134**, A566 (1964).

[55] N. F. Mott, Conduction in non-crystalline systems IX. the minimum metallic conductivity, Philosophical Magazine **26**, 1015 (1972).

[56] P. T. Brown, E. Guardado-Sanchez, B. M. Spar, E. W. Huang, T. P. Devereaux, and W. S. Bakr, Angle-resolved photoemission spectroscopy of a Fermi–Hubbard system, Nature Physics **16**, 26 (2020).

AUTHOR CONTRIBUTIONS:

ET, TPD, and SAK. conceived the study. ET developed the numerical code and performed the numerical calculations and data analysis. ET, VO, TPD, and SAK contributed to the interpretation of the results and development of the theoretical framework. ET and SAK wrote the manuscript with input from all authors.

COMPETING INTERESTS:

There are no competing interests to declare.

DATA AND MATERIALS AVAILABILITY:

The numerical data underlying all figures in the main text and the Supplementary Materials, together with the per-twist exact-diagonalization output from which they derive, are deposited in Zenodo https://doi.org/10.5281/zenodo.22565541.

Appendix A: Model, Hilbert space, symmetries, and boundary conditions

Here we briefly provide several basic definitions of the model and discussed observables and outline the structure of the code.

1. Model and Hilbert space

We study the infinite-U Hubbard model on finite clusters of the square lattice,

$$H \;=\; -t \sum_{\langle ij\rangle,\sigma} \left(\tilde{c}^{\dagger}_{i\sigma} \tilde{c}_{j\sigma} + \text{h.c.} \right), \qquad \tilde{c}_{i\sigma} = c_{i\sigma}\,(1 - n_{i\bar{\sigma}}), \tag{A1}$$

where the Gutzwiller-projected operators $\tilde{c}_{i\sigma}$ enforce the no-double-occupancy constraint, and the hole doping is $x = N_h/N$ with N_h the number of holes and N the number of sites. For fixed electron number $N_e = N - N_h$, the dimension of the constrained Hilbert space is $\binom{N}{N_h} 2^{N_e}$, i.e., the number of hole placements times the number of spin configurations of the remaining singly occupied sites.

The symmetries used in the calculation are: (i) $U(1)$ charge conservation, $[H, \hat{N}_e] = 0$; (ii) $SU(2)$ spin symmetry, $[H, \mathbf{S}] = 0$, of which we exploit S_z conservation together with the spin-flip degeneracy between $\pm S_z$ sectors, halving the number of blocks to be diagonalized; (iii) lattice translations, whose quantum numbers depend on the boundary conditions as specified below. Twists and staggering generically reduce the C_4 point group of the untwisted square clusters to C_2 or break it entirely; we therefore do not use point-group symmetries anywhere. The Hamiltonian is block diagonal in $(N_e, S_z, \mathbf{k})$, and each symmetry block is fully diagonalized with dense eigensolvers, retaining the complete many-body spectrum and all current matrix elements. The block structure and the largest dense-block dimensions are collected in Table I.

2. Cluster geometries

Three cluster geometries are used for the transport and thermodynamics results (Fig. 6): the 4×4 square torus, spanned by $\mathbf{L}_1 = (4, 0)$ and $\mathbf{L}_2 = (0, 4)$; the *staggered* 4×4 torus ($s = 1$), in which the y boundary is reconnected with a unit shift, $(x, N_y) \sim (x + s,\, 0)$, corresponding to $\mathbf{L}_2 = (-s, 4)$; and the 18-site tilted (Betts) cluster [37], spanned by $\mathbf{L}_1 = (3, 3)$ and $\mathbf{L}_2 = (3, -3)$. The 4×4 torus is well known to be a pathological geometry at the non-interacting level: its single-particle spectrum has a high degree of fine-tuned degeneracy, which collapses many-body levels onto a few distinct energies and enhances finite-size effects. Tilting (in the spirit of the Betts construction) and staggering modify the set of allowed momenta and lift these fine-tuned degeneracies; comparing the $s = 0$ and $s = 1$ sectors of the 4×4 cluster, and the 4×4 against the 18-site cluster, therefore provides independent finite-size diagnostics (App. C 3). The variational caging analysis of App. H additionally uses a 2×8 ladder with one hole.

3. Twisted and staggered boundary conditions

Twisted boundary conditions $\boldsymbol{\theta} = (\theta_x, \theta_y)$ are implemented by attaching phases to the hopping matrix elements, $t \to t\, e^{-i\boldsymbol{\theta}\cdot\boldsymbol{\delta}}$, with $\boldsymbol{\delta}$ the bond vector. For the simple torus the allowed momenta are

$$\mathbf{k}(\boldsymbol{\theta}) = \left(\frac{2\pi}{L_x}n_x + \theta_x,\ \frac{2\pi}{L_y}n_y + \theta_y\right), \tag{A2}$$

while on the staggered torus, $(x, N_y) \sim (x + s, 0)$,

$$\mathbf{k}(\boldsymbol{\theta}, s) = \left(\frac{2\pi}{L_x}n_x + \theta_x,\ \frac{2\pi}{L_y}\left(n_y + \frac{n_x s}{L_x}\right) + \theta_y\right). \tag{A3}$$

Equation (A3) satisfies the boundary conditions of the torus spanned by $\mathbf{L}_1 = (L_x, 0)$, $\mathbf{L}_2 = (-s, L_y)$: $\mathcal{T}_x^{L_x} = 1$ and $\mathcal{T}_y^{L_y}\mathcal{T}_x^{-s} = 1$. Because the twist enters only through the hopping phases, the eigenstates are strictly periodic on the torus, and the translation eigenvalues involve only the combination $\mathbf{k} - \boldsymbol{\theta}$. The closure conditions therefore require $(\mathbf{k} - \boldsymbol{\theta}) \cdot \mathbf{L}_{1,2} \in 2\pi\mathbb{Z}$, which Eq. (A3) satisfies for every twist:

$$(k_x - \theta_x)\, L_x = 2\pi n_x, \qquad (k_y - \theta_y)\, L_y - (k_x - \theta_x)\, s = 2\pi\left(n_y + \frac{n_x s}{L_x}\right) - \frac{2\pi n_x s}{L_x} = 2\pi n_y.$$

Staggering thus reshuffles the allowed momenta at fixed twist, so the $s = 0$ and $s = 1$ sectors provide independent finite-size samples.

For twist averaging we use a 5×5 "golden-ratio" grid,

$$\theta_x \in \left\{ \frac{2\pi(a+\varphi)}{5} \right\}_{a=0}^{4}, \qquad \theta_y \in \left\{ \frac{2\pi(b+\varphi)}{5} \right\}_{b=0}^{4}, \qquad \varphi = \frac{1+\sqrt{5}}{2}, \tag{A4}$$

i.e., 25 twists per boundary-condition sector. The irrational offset φ keeps every twist away from high-symmetry commensurate points, avoiding the fine-tuned degeneracies discussed above. The same grid is used for the 4×4 cluster in both boundary-condition sectors ($s = 0$ and $s = 1$) and, in full, for the 18-site cluster (25 twists); the $x = 3/16$ data shown in Fig. 4 are for a single irrational twist.

4. Numerical implementation

We use a custom Fortran exact-diagonalization code developed for this work. The code diagonalizes each dense symmetry block, and its structure is organized to make this full diagonalization and the subsequent spectral sums feasible at the sizes of Table I.

Each (N_e, S_z) sector is generated directly in the constrained (no-double-occupancy) Fock basis, with the Hamiltonian and current operators stored and applied sparsely. When an operator maps one basis state to another, the target index is found by binary search on a lexicographically sorted key map, e.g. a standard sorted-basis lookup, which keeps operator assembly near-linear in the sector dimension. Translation symmetry, carrying the attendant fermionic signs, then blocks each sector by lattice momentum $\mathbf{k}(\boldsymbol{\theta}, s)$; together with particle number and S_z (with the $\pm S_z$ degeneracy) this leaves a set of independent dense blocks whose largest dimension controls the cost and feasibility of the computation.

Every dense block is diagonalized in full on GPUs with the distributed multi-GPU eigensolver NVIDIA `cuSOLVERMp` [50]. The eigenpairs are then consumed in a single streaming pass, i.e., for each batch of eigenstates the current and kinetic-energy matrix elements are formed by sparse scatters and dense rotations, and their contributions to the conductivity and to the thermodynamic traces are accumulated on the fly, simultaneously for all temperatures, frequencies, and broadenings. The full spectral matrices are therefore never stored, which is what keeps the memory footprint manageable at the largest block sizes.

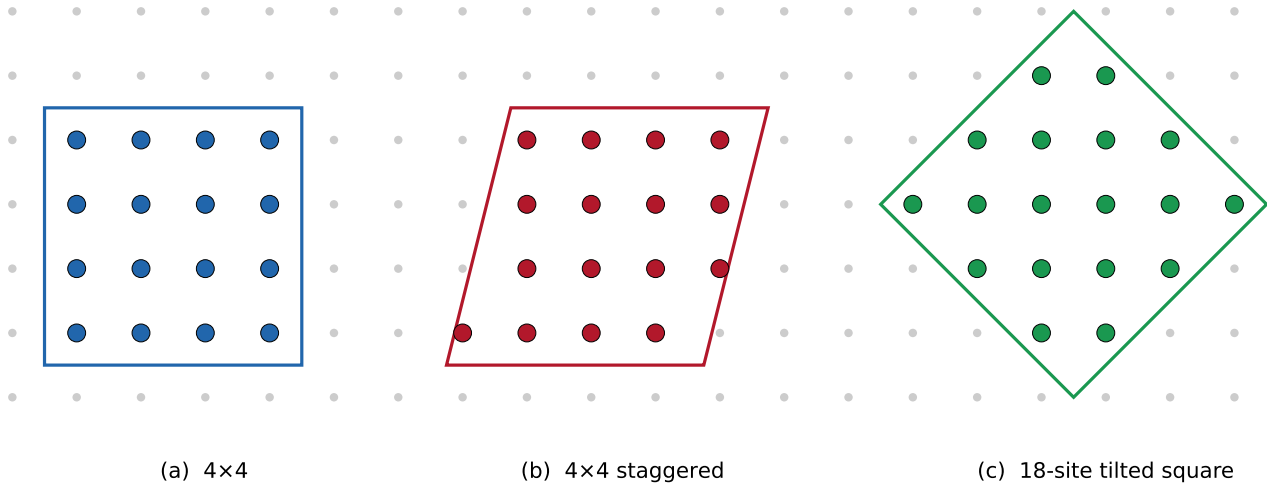


Figure 6. **Cluster geometries.** Representative finite clusters used in the exact-diagonalization calculations: (**a**) the 4×4 square torus, spanned by $\mathbf{L}_1 = (4,0)$, $\mathbf{L}_2 = (0,4)$; (**b**) the staggered 4×4 torus ($s = 1$), in which the y boundary is reconnected with a unit shift, $\mathbf{L}_2 = (-s,4)$, modifying the allowed momenta according to Eq. (A3); (**c**) the 18-site tilted square Betts cluster, $\mathbf{L}_1 = (3,3)$, $\mathbf{L}_2 = (3,-3)$.

Cluster	N_h	x	$\dim \mathcal{H}_{N_e}$	largest $(S_z, \mathbf{k})$ block	twists / role
4×4 ($s=0$ and $s=1$)	0	0	2^{16}	analytic, Eq. (B2)	χ_c reference
4×4 ($s=0$ and $s=1$)	1	1/16	524,288	6,435	25 twists
4×4 ($s=0$ and $s=1$)	2	2/16	1,966,080	25,740	25 twists
4×4	3	3/16	4,587,520	60,060	1 irrational twist; thermodynamics only
18-site Betts	0	0	2^{18}	analytic	χ_c reference
18-site Betts	1	1/18	2,359,296	24,310	25 twists; untwisted for spin-bond correlator
18-site Betts	2	2/18	10,027,008	109,430	1 irrational twist; thermodynamics only
4×5	1	1/20	10,485,760	92,378	25 twists
2×8 ladder	1	1/16	524,288	6,435	untwisted; caging analysis (App. H)

Table I. **Clusters, dopings, and Hilbert-space dimensions.** $\dim \mathcal{H}_{N_e} = \binom{N}{N_h} 2^{N_e}$ is the dimension of the constrained Hilbert space at fixed hole number; the largest dense block is the largest $(S_z, \mathbf{k})$ sector actually diagonalized (spin-flip degeneracy halves the number of S_z blocks). Common numerical parameters: temperature grid of 80 points, linear on $T \in [0.01, 2]\,t$; frequency grid of 201 points up to $\omega = 10\,t$, densified at low frequency; broadenings $\gamma/t \in \{0.005, 0.01, 0.02, 0.05, 0.1\}$.

Appendix B: Thermodynamic observables

All thermodynamic quantities are computed from the full spectra of the particle-number sectors. For each sector N_e and twist $\boldsymbol{\theta}$ the canonical partition function and free energy are

$$Z_{N_e}(T,\boldsymbol{\theta}) = \sum_n e^{-E_n(\boldsymbol{\theta})/T}, \qquad F_{N_e}(T,\boldsymbol{\theta}) = -T \ln Z_{N_e}(T,\boldsymbol{\theta}), \tag{B1}$$

with the sums running over all eigenstates of the sector. Unless stated otherwise, sector free energies and observables are averaged over the twist grid, Eq. (A4). The entropy and specific heat per site are obtained by numerical differentiation of the exact $F(T)$ and $E(T) = \langle H \rangle_T$ on the temperature grid, $S = -\partial F/\partial T/N$ and $C_V = \partial E/\partial T/N$. The uniform spin susceptibility is computed as in the main text, $\chi_s = (\langle S_z^2 \rangle - \langle S_z \rangle^2)/(NT)$.

The charge compressibility is obtained from the discrete second difference of the sector free energies with respect to the electron number,

$$\chi_c^{-1}(T) \;=\; N\Big[F_{N_e+1}(T) - 2F_{N_e}(T) + F_{N_e-1}(T)\Big], \tag{B2}$$

evaluated at the electron number N_e corresponding to the doping of interest. For the single-hole dopings the half-filled sector enters as one of the neighboring sectors; at $U = \infty$ it has no charge dynamics, so its free energy is exact, $F_N = -NT \ln 2$ (free spins). Concretely, $\chi_c(x{=}1/18)$ uses the 18-site sectors $N_e = 18, 17, 16$, $\chi_c(x{=}1/16)$ uses the 4×4 sectors $N_e = 16, 15, 14$, and $\chi_c(x{=}2/16)$ uses $N_e = 15, 14, 13$. Each sector free energy is averaged over its available twists (Table I): all 4×4 sectors with $N_h \leq 2$ and the 18-site one-hole sector use the full 25-twist grid, while the outermost sectors of the $x = 1/18$ and $x = 2/16$ differences ($N_e = 16$ on the 18-site cluster and $N_e = 13$ on the 4×4 cluster) are available for a single twist.

Appendix C: Optical conductivity and the dc limit

1. Kubo formula and broadening

The longitudinal optical conductivity is computed from the Lehmann representation,

$$\sigma_\mu(\omega) \;=\; \pi \, \frac{1 - e^{-\omega/T}}{\omega} \sum_{n,m} \frac{e^{-E_n/T}}{Z} \; |\langle m|J_\mu|n\rangle|^2 \, \delta\big(\omega - (E_m - E_n)\big), \qquad \mu = x, y, \tag{C1}$$

with J_μ the (projected) current operator, using every eigenstate and every current matrix element of each symmetry block. Here and throughout the appendices, $\sigma(\omega)$ denotes the real (dissipative) part

of the conductivity, and the reported conductivity is the average of the two diagonal components, $\sigma = (\sigma_x + \sigma_y)/2$ (the anisotropy is at most a few percent in the staggered-BC case).

The delta functions are broadened into Lorentzians, $\delta(\omega - \Delta E) \to \frac{1}{\pi}\,\gamma/[\gamma^2 + (\omega - \Delta E)^2]$, and the calculation is repeated for $\gamma/t \in \{0.005, 0.01, 0.02, 0.05, 0.1\}$. The physically meaningful broadening window is bounded below by the finite-size level spacing and above by the temperature, $\Delta_{\mathrm{fs}} \lesssim \gamma \ll T$: for smaller γ the spectrum resolves into discrete peaks, while larger γ artificially redistributes spectral weight. In practice, to minimize the systematic loss of spectral weight caused by introducing broadening, we take the $\gamma \to 0$ limit by linear extrapolation in γ from the two smallest values, $\sigma(\omega, \gamma) = \sigma_0(\omega) + a_\omega \gamma + \mathcal{O}(\gamma^2)$. The results obtained are robust to other extrapolation schemes, e.g., using more broadening values or adding higher order terms in γ. Representative extrapolations for both clusters are shown in Fig. 7(a,b), and Fig. 7(c,d) shows the resulting dc resistivity obtained from the fixed-broadening spectra alongside the $\gamma \to 0$ extrapolation. In all cases we find that the γ dependence is regular and enables a systematic extrapolation.

We also note that the residual resistivity obtained from extrapolating the T-linear resistivity in the semi-quantum regime to $T = 0$ is reduced for larger systems (see Fig. 2), which suggests it is a finite-size artifact.

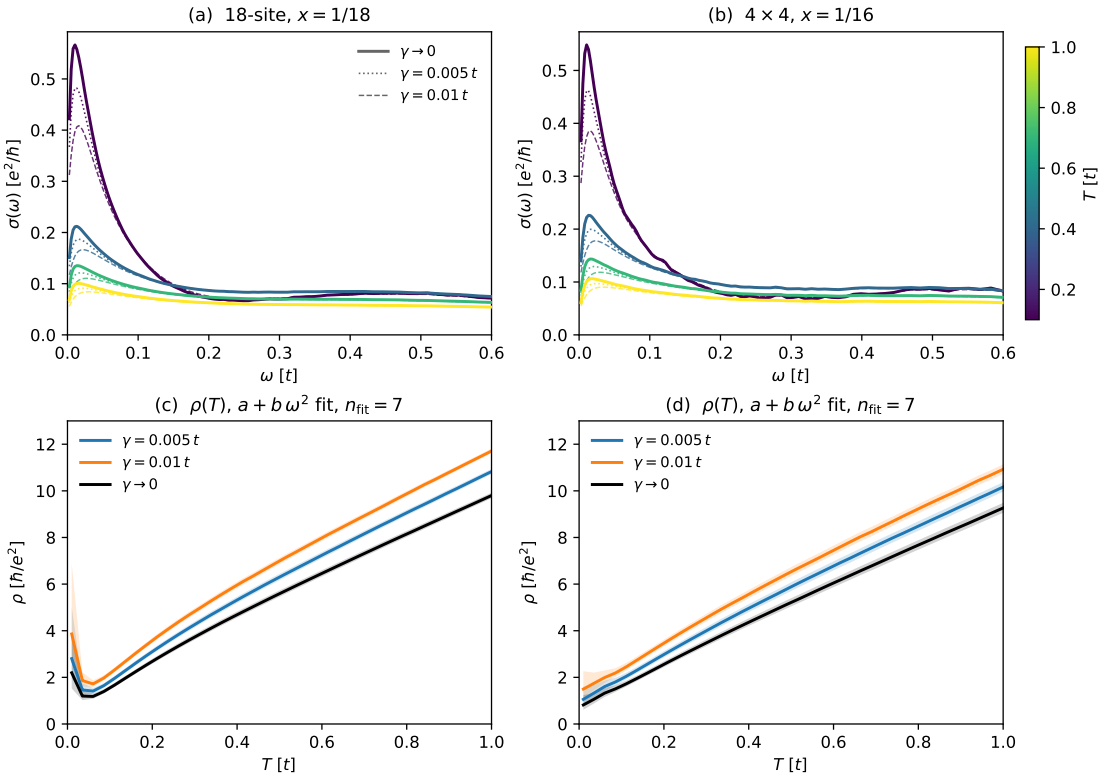


Figure 7. $\gamma \to 0$ **extrapolation of the optical conductivity and the dc resistivity.** (**a**) and (**b**) Optical conductivity at representative temperatures for the sampled broadenings $\gamma/t = 0.005, 0.01$, together with the $\gamma \to 0$ extrapolation from the two smallest values, for the 18-sites and 4×4 clusters, respectively. (**c**) and (**d**) dc resistivity obtained by applying the extraction of App. C 2 to the fixed-broadening spectra with $\gamma = 0.005\,t$ and $0.01\,t$ and to the $\gamma \to 0$-extrapolated spectra. Twist error becomes significant below $T \lesssim 0.08t$, indicating increased sensitivity to finite size effects, similarly to the non-staggered/staggered comparison in the main text.

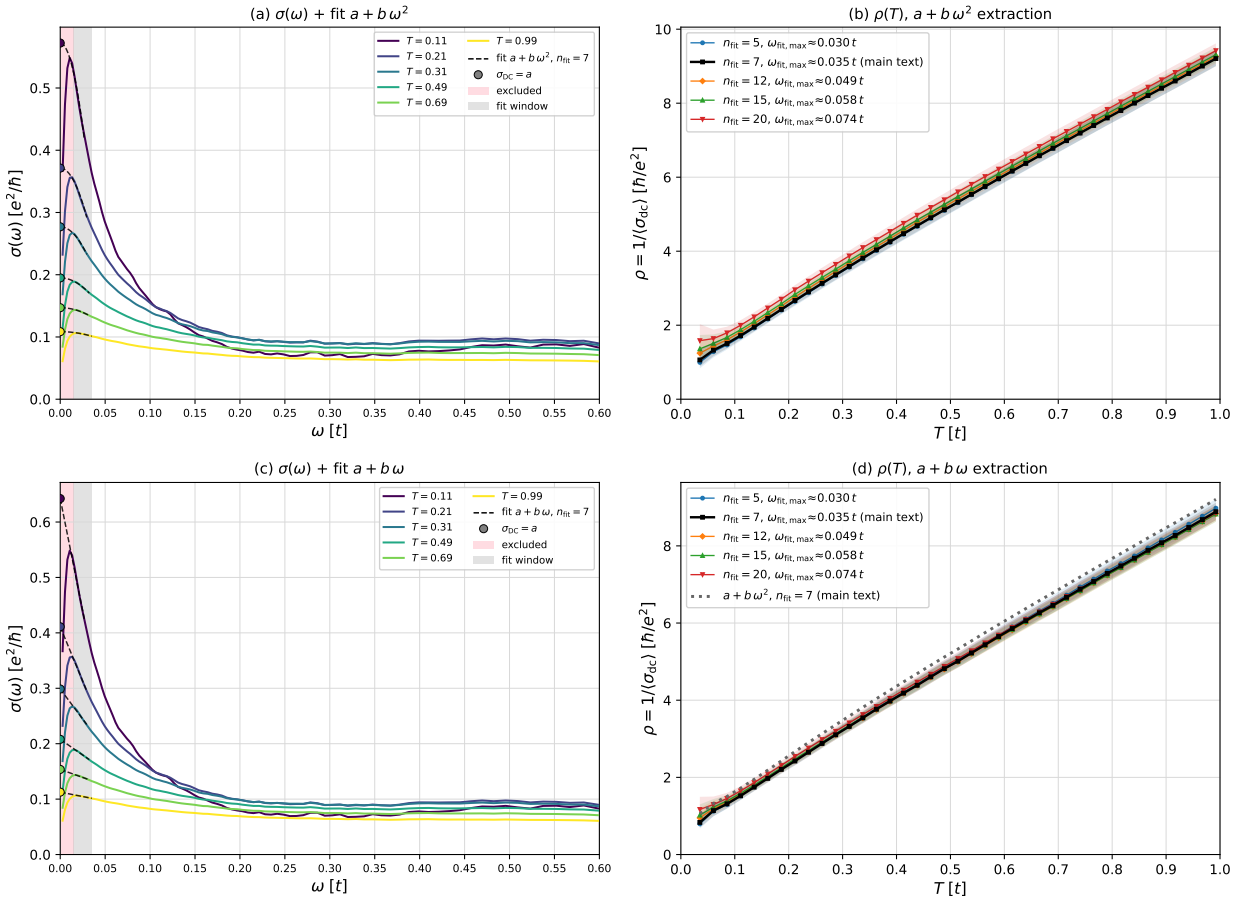


Figure 8. **Extraction of the dc conductivity and its robustness in representative case** 4×4**,** $x = 1/16$**.** (**a**) Twist-averaged, $\gamma \to 0$-extrapolated $\sigma(\omega)$ at representative temperatures. The pink band marks the level-repulsion downturn at $\omega < \omega_{\mathrm{peak}}$, excluded from the fit; the gray band marks the fit window $[\omega_{\mathrm{peak}}, \omega_{\mathrm{fit,max}}]$ used for the quadratic extrapolation $\sigma(\omega) = \sigma_{\mathrm{dc}} + b\,\omega^2$ (dashed lines; circles mark the extracted $\sigma_{\mathrm{dc}} = a$ at $\omega = 0$). (**b**) Twist-averaged resistivity $\rho(T) = 1/\langle\sigma_{\mathrm{dc}}\rangle_{\boldsymbol{\theta}}$ from the quadratic fit for several fit windows, labeled by their upper frequency $\omega_{\mathrm{fit,max}} \approx 0.03$–$0.07\,t$; the main-text choice is $\omega_{\mathrm{fit,max}} \approx 0.05\,t$. Bands show $1/(\langle\sigma_{\mathrm{dc}}\rangle \mp \mathrm{SEM})$ over the twists. (**c**,**d**) The same, using a *linear* extrapolation $\sigma(\omega) = \sigma_{\mathrm{dc}} + b\,\omega$; panel (**d**) overlays the quadratic main-text result (dotted). The two fit forms differ by a modest offset (~ 10, largest near $0.08t$, below which twist variance grows rapidly and finite-size effects dominate) but give the same T-linear slope, and within each form the fit window changes $\rho(T)$ by no more than about the twist standard error for $T > T_{\mathrm{fs}}$.

2. Extraction of the dc limit

At the lowest frequencies the finite cluster deviates from the expected regular $\omega \to 0$ behavior of the thermodynamic limit as finite cluster artifacts depletes the spectral weight in a narrow window

near $\omega = 0$, producing a downturn of $\sigma(\omega)$ below a temperature-dependent scale $\omega_{\rm peak}$ [31]. We therefore extract $\sigma_{\rm dc}$ by excluding the downturn window and fitting

$$\sigma(\omega) \;=\; \sigma_{\rm dc} + b\,\omega^2, \qquad \omega \in [\omega_{\rm peak},\, \omega_{\rm fit,max}], \tag{C2}$$

where $\omega_{\rm peak}$ is the local maximum of the per-twist, $\gamma \to 0$-extrapolated $\sigma(\omega)$ near $\omega = 0$, and the fit window extends to $\omega_{\rm fit,max} \approx 0.05\,t$ in the main text. The extraction is performed independently for each twist, and the resistivity is obtained from the twist-averaged conductivity, $\rho(T) = 1/\langle\sigma_{\rm dc}(\boldsymbol{\theta})\rangle_{\boldsymbol{\theta}}$, with the uncertainty band propagated from the standard error of $\langle\sigma_{\rm dc}\rangle$, i.e. $\rho_\pm = 1/(\langle\sigma_{\rm dc}\rangle \mp \mathrm{SEM})$. The extraction can be done when the excluded window is small compared with the physical scales, $\max(\omega_{\rm peak}, \gamma) \ll \min(T, t)$, which is satisfied throughout the reported temperature range.

Figure 8 tests the stability of this procedure. Varying the fit window over $\omega_{\rm fit,max} \approx 0.03$–$0.07\,t$ [Fig. 8(b)] changes $\rho(T)$ by no more than about the twist standard error for $T > T_{\rm fs}$. Replacing the quadratic fit by a linear one, $\sigma(\omega) = \sigma_{\rm dc} + b\,\omega$ [Fig. 8(c,d)], shifts $\rho(T)$ downward by a small constant amount but leaves the T-linear slope essentially unchanged. The characteristics of the semi-quantum regime discussed in the main text, i.e., the magnitude of ρ, its approximate T-linearity, and its slope, are thus insensitive both to the fit window and to the fit form.

3. More details on finite size effects

We further assess the finite-size dependence of the transport results in Fig. 9. Panel (a) shows the residual resistivity ρ_0, obtained from a linear fit $\rho(T) = \rho_0 + AT$ over the temperature window indicated in the caption; the results are insensitive to moderate changes of this window. In the one-hole sector, ρ_0 decreases systematically upon increasing the system size from $N = 16$ to 18 and 20. Although the doping simultaneously decreases along this sequence, the systematic suppression with system size suggests that the nonzero intercept is predominantly a finite-size effect, consistent with its disappearance toward the thermodynamic limit. The two-hole $N = 16$ result has a substantially larger intercept, indicating stronger finite-size corrections in this sector.

In contrast, the slope of the T-linear resistivity is considerably more stable. At low doping, where $\rho \sim T/x$ is expected, panel (b) shows xA. The one-hole results are nearly independent of system size, even as the doping changes from $x = 1/16$ to $1/20$, as expected for $\rho \sim T/x$. Thus, while the residual resistivity is progressively suppressed with increasing size, the T-linear slope retains the expected $1/x$ scaling. This stability suggests that the slope is an intrinsic property of the semi-quantum regime rather than a finite-size artifact. The two-hole result exhibits a larger

correction, consistent with the stronger size sensitivity seen in panel (a), but remains qualitatively consistent with the dilute one-hole results.

A separate finite-size feature appears in the low-frequency optical conductivity. We characterize the small downturn as $\omega \to 0$ by the position of the low-frequency maximum of $\sigma(\omega)$, denoted ω^*. As shown in panel (c), $\omega^*/T \lesssim 1$ for $T \gtrsim 0.08t$, encompassing most of the semi-quantum regime. The downturn is therefore confined to a frequency scale well below the thermal scale over the regime of interest. This separation of scales, together with the agreement between the different extrapolation procedures discussed above, shows that the extracted dc conductivity is insensitive to this narrow low-frequency feature. Again, the two-hole sector shows larger low-temperature corrections while following the same overall trend.

Finally, panel (d) shows the fraction of spectral weight not contained in the regular part of the optical conductivity,

$$f_D = 1 - \frac{\int_{0^+}^{\infty} d\omega\, \sigma(\omega)}{(\pi/2)|K|}, \tag{C3}$$

i.e., the Drude-weight fraction, which in the present context is a finite-size contribution that decreases systematically with increasing system size, remaining below 20% over the regime of interest, consistent with its expected vanishing in the thermodynamic limit. Here $(\pi/2)|K|$ is the total optical weight on the half-axis $\omega \geq 0$, with K the thermodynamic kinetic energy per site. A finite zero-frequency contribution is a well-known artifact of optical-conductivity calculations on finite clusters with twisted boundary conditions [51–53]: the many-body spectrum remains sensitive to flux threaded through the finite torus, giving a finite charge stiffness and hence a $\delta(\omega)$ peak, physically corresponding to persistent currents. Note that this zero-frequency contribution does not enter our determination of σ_{dc}, which is obtained by extrapolating the regular conductivity using data at $\omega \gtrsim \omega^*$, thereby excluding both the spurious low-frequency downturn and the $\omega = 0$ Drude contribution. The missing weight in panel (d) therefore does not correspond to unresolved finite-frequency transitions contaminating the dc limit; moreover, its systematic decrease with system size indicates that this weight redistributes, in the thermodynamic limit, to frequencies captured by the regular part. Finite-size effects relevant to σ_{dc} are instead assessed in the main text through system-size dependence, boundary-condition comparisons, and the variance over twists.

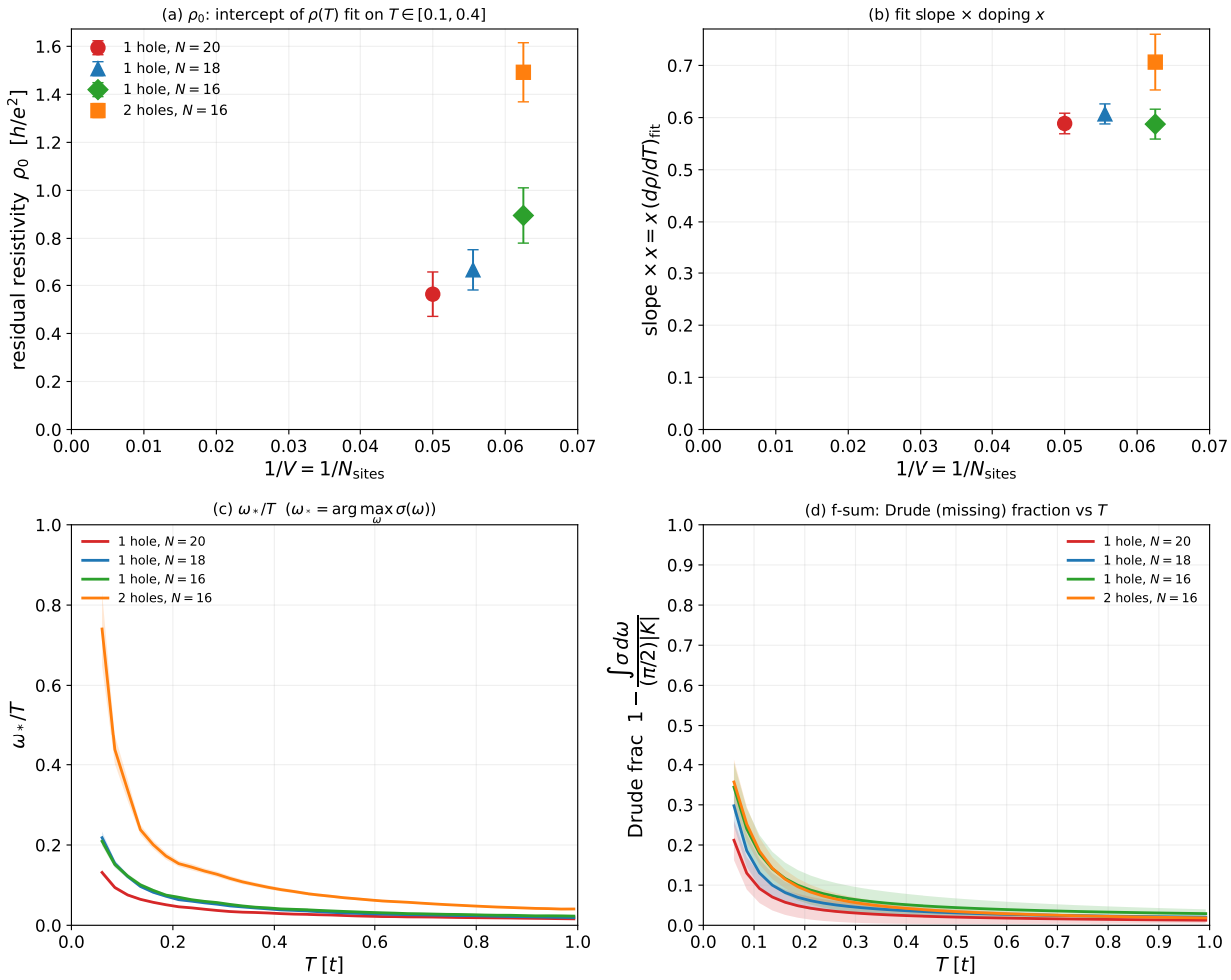


Figure 9. **Finite-size diagnostics of charge transport.** (A) Residual resistivity ρ_0 obtained from fits $\rho(T) = \rho_0 + AT$ over $0.1 \leq T/t \leq 0.4$, shown versus inverse system size. (B) Corresponding slope A multiplied by the doping x, testing the expected low-doping scaling $\rho \sim T/x$. (C) Position ω^* of the low-frequency maximum of $\sigma(\omega)$, normalized by T. (D) Drude-weight fraction, defined as the spectral weight missing from the regular optical conductivity. Results are shown for one hole on $N = 16, 18, 20$ clusters and two holes on $N = 16$.

4. Optical lineshape diagnostics

To characterize the narrowing of the low-frequency feature without assuming a specific lineshape, we define $\Delta\sigma(\omega, T) = \sigma(\omega, T) - \sigma(\omega, T_{\mathrm{ref}})$. We characterize its frequency extent by the high-frequency half-maximum edge $\Delta\omega$, defined by

$$\Delta\sigma(\Delta\omega, T) = \tfrac{1}{2}\Delta\sigma_{\mathrm{dc}}(T), \qquad \Delta\omega > \omega_{\mathrm{max}},$$

where $\omega_{\max}$ is the position of the maximum of $\Delta\sigma(\omega, T)$ [Fig. 10A]. In the main text we use $T_{\mathrm{ref}} = t$; the resulting $\Delta\omega(T)$ is shown in Fig. 3F.

We test the dependence of this construction on the choice of reference temperature in Fig. 10B. Solid and dashed curves show the raw $\Delta\omega(T)$ obtained using $T_{\mathrm{ref}} = t$ and $2t$, respectively. Changing T_{ref} shifts the absolute values somewhat while leaving the qualitative temperature dependence essentially unchanged. Unlike in Fig. 3F, the $x = 2/16$ values are shown here without the factor of $1/2$, so that the absolute frequency scale can be compared directly. The one-hole clusters exhibit an approximately linear decrease of $\Delta\omega$ upon cooling, whereas the two-hole result has a larger characteristic frequency scale and a qualitatively different temperature dependence, as discussed in the main text.

As a further check that $\Delta\omega$ meaningfully characterizes the low-frequency lineshape, Figs. 10C–E show $\Delta\sigma(\omega, T)/\Delta\sigma_{\mathrm{dc}}(T)$ versus $\omega/\Delta\omega(T)$ at representative temperatures. The peak height and high-frequency half-maximum point coincide by construction. Away from these normalization points, the one-hole curves exhibit an approximate lineshape collapse over a broader frequency range, while the two-hole lineshape shows larger deviations, consistent with its qualitatively distinct behavior.

5. Ioffe–Regel convention

For reference we state the convention used for the Ioffe–Regel line in the main text. For a two-dimensional Drude metal,

$$\sigma = \frac{e^2 n \tau}{m} = \frac{e^2}{2\pi\hbar}\, k_F \ell. \tag{C4}$$

The validity of the Boltzmann transport equation (for Fermi liquids or non-Fermi liquids [54]) requires the mean free path to exceed the Fermi wavelength, $\ell \gtrsim \lambda_F = 2\pi/k_F$, i.e., $k_F\ell/2\pi \gtrsim 1$, which translates into

$$\sigma_{\mathrm{IR}} = \frac{e^2}{\hbar} \qquad \Longleftrightarrow \qquad \rho_{\mathrm{IR}} = \frac{\hbar}{e^2}. \tag{C5}$$

Resistivities $\rho \gtrsim \hbar/e^2$ therefore signal transport beyond the Boltzmann transport regime and in particular do not host electronic quasiparticles. Note that this criterion is distinct from the Mott criterion $\ell > a$ [55], which is violated only at correspondingly larger resistivities.

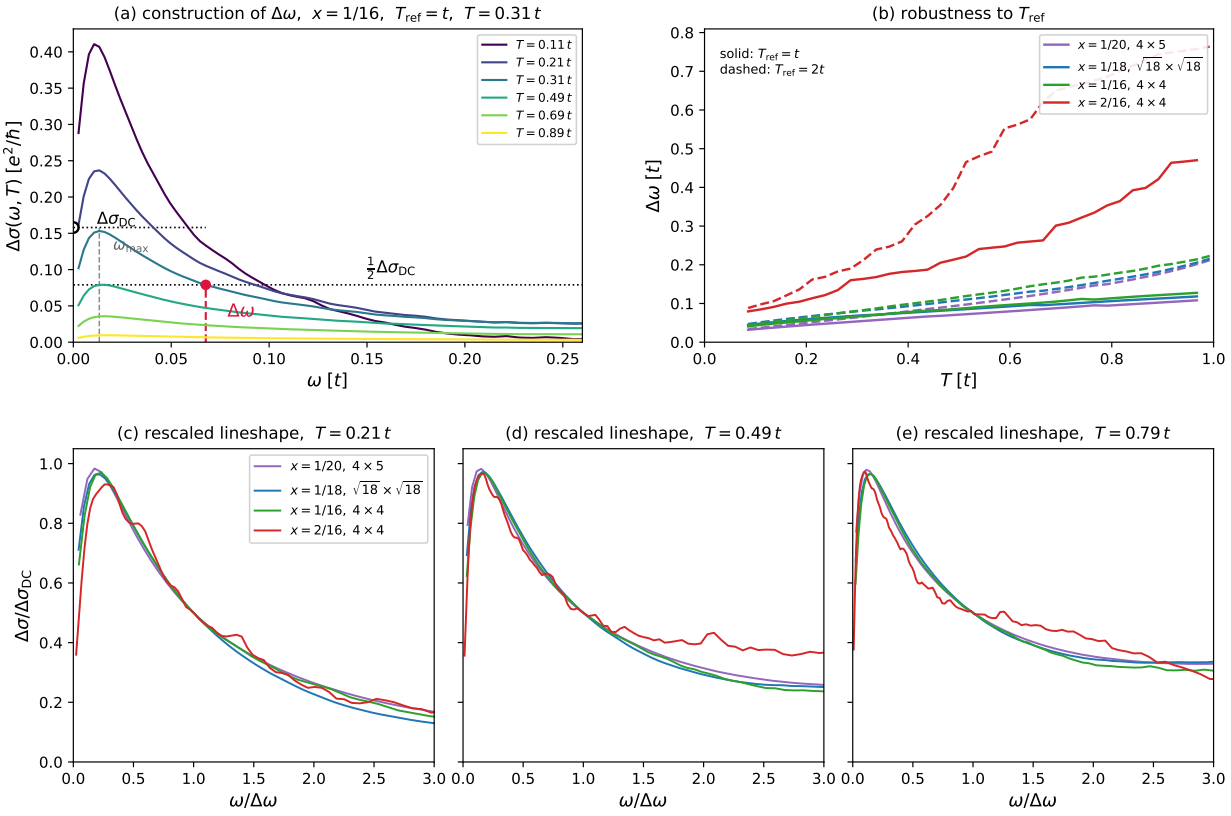


Figure 10. **Characterization of the low-frequency optical feature.** (A) Construction of the high-frequency half-maximum edge $\Delta\omega$ from $\Delta\sigma(\omega,T) = \sigma(\omega,T) - \sigma(\omega,T_{\rm ref})$ for $x = 1/16$ and $T_{\rm ref} = t$. The marked points indicate $\omega_{\rm max}$ and the high-frequency half-maximum crossing $\Delta\omega$. (B) Dependence on the reference temperature. Solid and dashed curves show the raw $\Delta\omega(T)$ obtained using $T_{\rm ref} = t$ and $2t$, respectively, for the four systems shown in Fig. 3. The $x = 2/16$ values are shown without the factor of $1/2$ used for visual comparison in Fig. 3F. (C–E) Rescaled low-frequency lineshapes, $\Delta\sigma(\omega,T)/\Delta\sigma_{\rm dc}(T)$ versus $\omega/\Delta\omega(T)$, at the indicated representative temperatures.

Appendix D: Resistivity in a bubble approximation

Here we provide a limited examination of the importance of vertex corrections to the resistivity by comparing the full Kubo result with the "bubble" conductivity constructed from the single-particle spectral function. We restrict this comparison to the 4×4 cluster with one hole, $x = 1/16$. We compute the exact canonical finite-T *spin-summed* spectral function of the projected electrons

$$\tilde{c}_{\boldsymbol{k}\sigma} = \frac{1}{\sqrt{N}} \sum_j e^{-i\boldsymbol{k}\cdot\boldsymbol{r}_j} c_{j\sigma}(1 - n_{j\bar{\sigma}}) \tag{D1}$$

by full diagonalization of the N_e-1, N_e, and N_e+1 sectors,

$$A(\boldsymbol{k},\omega,T)=\sum_{\sigma,n,m}\frac{e^{-E_n^{(N_e)}/T}}{Z_{N_e}}\Big[|\langle m^{(N_e-1)}|\tilde{c}_{\boldsymbol{k}\sigma}|n^{(N_e)}\rangle|^2\delta_\gamma\Big[\omega-(E_n^{(N_e)}-E_m^{(N_e-1)})\Big] \\ +|\langle m^{(N_e+1)}|\tilde{c}^\dagger_{\boldsymbol{k}\sigma}|n^{(N_e)}\rangle|^2\delta_\gamma\Big[\omega-(E_m^{(N_e+1)}-E_n^{(N_e)})\Big]\Big]. \tag{D2}$$

Here δ_γ is a Lorentzian broadening. Frequencies are not shifted by the chemical potential, so that the Fermi level occurs at $\omega=\mu(T)$. The projected spectral function obeys $\int d\omega\, A(\boldsymbol{k},\omega,T)=2-n=1+x$, giving 17/16 for the cluster considered here.

From $A(\boldsymbol{k},\omega,T)$ we evaluate the dc bubble conductivity [23],

$$\sigma_x^{\rm bub}(T)=\frac{\pi}{N}\sum_{\boldsymbol{k}}(v_{\boldsymbol{k}}^x)^2\int d\omega\,\left(-\frac{\partial f(\omega-\mu)}{\partial\omega}\right)\frac{A(\boldsymbol{k},\omega,T)^2}{2}, \tag{D3}$$

where $v_{\boldsymbol{k}}^x=2t\sin\tilde{k}_x$. The factor 1/2 follows from $\sum_\sigma A_\sigma^2=A^2/2$ for the spin-summed spectral function in the spin-symmetric state.

Because this comparison is not the primary focus of the present work and carries a substantially higher computational cost, we restrict the calculation to four boundary twists and a coarser frequency grid. This provides meaningful results for $T\gtrsim 0.2t$, sufficient for the limited purpose here of assessing the role of vertex corrections. Since $A(\boldsymbol{k},\omega,T)$ is evaluated canonically whereas Eq. (D3) contains a grand-canonical Fermi window, for each twist we determine μ from

$$\sum_{\boldsymbol{k}}\int d\omega\, f(\omega-\mu)A(\boldsymbol{k},\omega,T)=N_e \tag{D4}$$

with f the Fermi-Dirac distribution function. We restrict the comparison to temperatures for which the thermally sampled window of width $\sim T$ around μ is sufficiently broad that finite-size ambiguities in the precise location of the chemical potential are unimportant.

Figure 11 shows the resulting bubble resistivity together with the full Kubo result, alongside representative single-particle spectral functions entering Eq. (D3). The bubble resistivity, $\rho^{\rm bub}=1/\langle\sigma^{\rm bub}\rangle_{\boldsymbol{\theta}}$, differs quantitatively from the full Kubo resistivity of the finite cluster, while exhibiting a similar temperature dependence. Over $0.3\lesssim T/t\leq 2$,

$$\frac{\rho^{\rm bub}(T)}{\rho^{\rm Kubo}(T)}\approx 1.6, \tag{D5}$$

with little detectable temperature dependence. Thus we find that vertex corrections are important for quantitatively capturing the finite-cluster resistivity, although the bubble shows similar T-scaling over this range. The importance of such corrections is consistent with the quantitative discrepancy between 16-site FTLM and single-site DMFT resistivities reported for the doped Hubbard

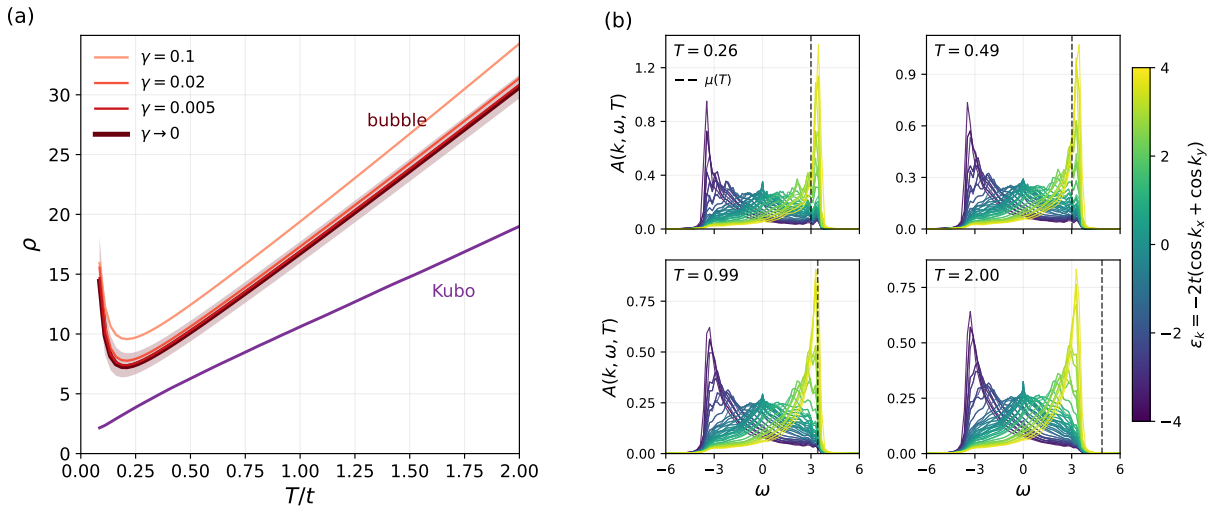


Figure 11. **Single-particle spectral function and bubble resistivity.** (**a**) Full Kubo resistivity and the vertex-free bubble resistivity ρ^{bub} obtained from Eq. (D3) for the 4×4 one-hole cluster. (**b**) Spin-summed spectral function $A(\boldsymbol{k}, \omega, T)$ entering Eq. (D3), shown for $\gamma = 0.02t$ at four representative temperatures. Curves correspond to the 64 twist-shifted momenta obtained by pooling the 16 momenta from each of the four boundary twists used in the bubble calculation; the curves are not averaged over twists. Lines are colored by the bare-band energy $\varepsilon_{\boldsymbol{k}} = -2t(\cos k_x + \cos k_y)$ of the corresponding twist-shifted momentum. Frequencies are not shifted by the chemical potential, and dashed vertical lines indicate $\mu(T)$ determined from Eq. (D4).

model in Ref. [12]. We defer a systematic study of these effects and a more detailed investigation of the single-particle spectral function, which is directly accessible in cold-atom Fermi–Hubbard systems through ARPES-type measurements [56], to future work.

Appendix E: Details on the hole-spin-bond correlator

1. Definition and normalization

Recall the connected hole-spin-bond correlator defined in Eq. (2) is

$$C_h(\mathbf{R}, \mathbf{e}; T) = \left\langle \rho_h(\mathbf{0})\, \mathbf{S}_{\mathbf{R}-\mathbf{e}/2} \cdot \mathbf{S}_{\mathbf{R}+\mathbf{e}/2} \right\rangle - \langle \rho_h(\mathbf{0}) \rangle \left\langle \mathbf{S}_{\mathbf{R}-\mathbf{e}/2} \cdot \mathbf{S}_{\mathbf{R}+\mathbf{e}/2} \right\rangle, \qquad \langle \rho_h(\mathbf{0}) \rangle = x = \frac{1}{N}, \quad \text{(E1)}$$

where $\mathbf{R}$ is the shortest displacement, accounting for periodic boundary conditions, from the origin to the bond center, and $\mathbf{e} = \hat{\mathbf{x}}, \hat{\mathbf{y}}$ specifies the bond orientation. We denote by $C_h(R, T)$ the value of C_h at $R = |\mathbf{R}|$. We normalize throughout by

$$C_0 = \frac{x^2}{2}, \quad \text{(E2)}$$

the $T \to 0$ value of (E1) on any bond away from the hole, derived below. The four $R = 1/2$ bonds incident on the conditioned hole site are called *incident*.

2. A sum rule

For brevity we denote $b = (i, i + \mathbf{e})$ the nearest-neighbor bond and $B = \sum_b \mathbf{S}_i \cdot \mathbf{S}_{i+\mathbf{e}}$ the total nearest-neighbor bond operator, with the sum running over all $2N$ bonds. With exactly one hole, $\sum_{\mathbf{r}} \rho_h(\mathbf{r}) = 1$ as an operator identity, while both B and the thermal state are translation invariant. Hence

$$\langle \rho_h(\mathbf{0}) B \rangle = \frac{1}{N} \sum_{\mathbf{r}} \langle \rho_h(\mathbf{r}) B \rangle = \frac{1}{N} \langle B \rangle = x \langle B \rangle. \tag{E3}$$

Summing (E1) over all bonds therefore gives

$$\sum_b C_h(b; T) = \langle \rho_h(\mathbf{0}) B \rangle - x \langle B \rangle = 0, \tag{E4}$$

where $C_h(b; T)$ is shorthand for $C_h(\mathbf{R}_b, \mathbf{e}_b; T)$.

3. The Nagaoka ground state

As $T \to 0$, the $U = \infty$ one-hole ground state is the Nagaoka ferromagnet [33], with maximal total spin $S = (N - 1)/2$ and a uniformly delocalized hole, so that $\langle \rho_h(\mathbf{r}) \rangle = x$ for every $\mathbf{r}$. Two elementary observations then fix (E1) completely.

First, conditioned on the hole sitting at the origin, all remaining spins belong to the maximally polarized $S = (N - 1)/2$ multiplet. Hence, on any bond that avoids the origin,

$$\langle \mathbf{S}_i \cdot \mathbf{S}_{i+\mathbf{e}} \rangle_h = \frac{1}{4}, \tag{E5}$$

i.e.

$$\langle \rho_h(\mathbf{0})\, \mathbf{S}_i \cdot \mathbf{S}_{i+\mathbf{e}} \rangle = \frac{x}{4}. \tag{E6}$$

On an incident bond one endpoint is the conditioned hole site and therefore carries no spin, so the joint expectation vanishes identically as an operator identity.

Second, without conditioning on the hole position, either endpoint of a given bond is empty with probability x, so the probability that both endpoints are occupied is $1 - 2x$. In the fully polarized state this gives

$$\langle \mathbf{S}_i \cdot \mathbf{S}_{i+\mathbf{e}} \rangle = \frac{1}{4}(1 - 2x). \tag{E7}$$

Combining the two, the $T \to 0$ values are

$$C_h^{\text{non-inc}} = \frac{x}{4} - x\,\frac{1-2x}{4} = \frac{x^2}{2} = C_0, \qquad \frac{C_h(R=1/2, T\to 0)}{C_0} = \frac{-x(1-2x)/4}{x^2/2} = -\frac{1-2x}{2x}, \tag{E8}$$

which is -8 for $N = 18$. The first of these is Eq. (E2): in the fully polarized state the normalized correlator on every non-incident bond is exactly $+1$, independently of N and of its distance from the hole. The two limits in (E8) are not independent: with 4 incident and $2N-4$ non-incident bonds, the sum rule (E4) requires

$$4 \times \left[-\frac{N-2}{2}\right] + (2N-4) \times 1 = 0, \tag{E9}$$

which holds identically.

The incident shell is special because it contains no conditional local bond information. Since the conditional part vanishes there identically, (E1) reduces to minus the disconnected piece alone. Defining the orientation-averaged nearest-neighbor spin correlation by

$$\langle \mathbf{S}_i \cdot \mathbf{S}_{i+\mathbf{e}} \rangle_{\text{nn}} \equiv \frac{1}{2} \sum_{\mathbf{e}=\hat{\mathbf{x}},\hat{\mathbf{y}}} \langle \mathbf{S}_i \cdot \mathbf{S}_{i+\mathbf{e}} \rangle\,, \tag{E10}$$

the shell-averaged incident correlator obeys the exact identity

$$\frac{C_h(R=1/2, T)}{C_0} = -\frac{2}{x}\,\langle \mathbf{S}_i \cdot \mathbf{S}_{i+\mathbf{e}} \rangle_{\text{nn}} \qquad \text{at all } T. \tag{E11}$$

The deep blue column at $R = 1/2$ in Fig. 5A is therefore not a statement about the local bonds surrounding a conditioned hole; it directly tracks the global nearest-neighbor spin correlation, up to rescaling.

4. Formation of the ferromagnetic texture

Fig. 12A shows the five non-incident shells. All approach the common Nagaoka value $+1$ as $T \to 0$, but their evolution is quite different. The $R = \sqrt{5}/2$ shell, consisting of the eight bonds forming the 3×3 "spin cage" around the hole, is the only one that overshoots this value, peaking at intermediate T inside the semi-quantum regime. The more distant shells instead become negative at intermediate temperature. By the sum rule (E4), any enhancement of the connected correlation near the hole must be compensated elsewhere.

Since C_h also contains a temperature-dependent disconnected contribution, the overshoot above $+1$ does not mean that the local bond correlation exceeds that of the fully polarized state. To characterize the local texture more directly, we consider the conditional bond correlation

$$\langle \mathbf{S}_i \cdot \mathbf{S}_{i+\mathbf{e}} \rangle_h \equiv \frac{\langle \rho_h(\mathbf{0})\, \mathbf{S}_i \cdot \mathbf{S}_{i+\mathbf{e}} \rangle}{x}, \tag{E12}$$

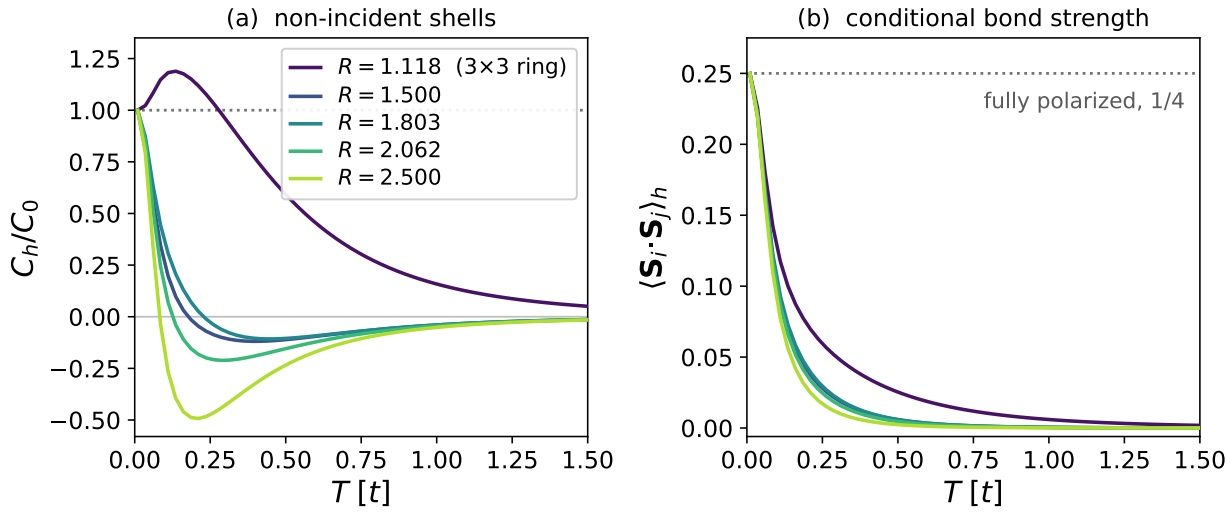


Figure 12. **Shell-resolved hole-spin-bond correlator, 18-site cluster, $x = 1/18$, untwisted.** Bonds are grouped by the distance R from the hole to the bond center; the incident shell $R = 1/2$, fixed exactly by Eq. (E11), is not shown. (**a**) C_h/C_0, Eq. (E1) normalized by its Nagaoka value $C_0 = x^2/2$ (dotted). (**b**) The conditional bond strength $\langle \mathbf{S}_i \cdot \mathbf{S}_j \rangle_h = \langle \rho_h(0)\, \mathbf{S}_i \cdot \mathbf{S}_j \rangle / x$, same shells and colors, approaching the fully polarized 1/4 (dotted).

shown in Fig. 12B. It vanishes identically on the incident shell, approaches the fully polarized value 1/4 on all other shells as $T \to 0$, and is largest on the $R = \sqrt{5}/2$ ring. Its magnitude, however, remains unsaturated down to very low temperatures. In other words, below T_{quant}, the spins near the hole are clearly correlated ferromagnetically, but the local texture remains fluctuating and rather than fully polarized.

Appendix F: High-temperature expansions

The dashed high-temperature curves in the main-text figures (Figs. 2B and 4) follow from the leading high-temperature expansion (HTE) of the free energy, which we summarize here. At $T \gg t$ the canonical partition function of a cluster of V sites with N_e electrons is expanded as

$$Z_{N_e} = \Omega_{N_e} \left(1 - \beta \langle H \rangle_0 + \tfrac{\beta^2}{2} \langle H^2 \rangle_0 + \dots \right), \qquad \Omega_{N_e} = \binom{V}{N_e} 2^{N_e}, \tag{F1}$$

where $\langle \cdot \rangle_0$ denotes the infinite-temperature average and Ω_{N_e} counts the constrained configurations. Since H is purely off-diagonal in the occupation basis, $\langle H \rangle_0 = 0$; moreover $\langle H^3 \rangle_0 = 0$ on the bipartite clusters (the 4×4 torus and the 18-site Betts cluster), because their shortest closed loops are the four-bond plaquettes. The one caveat concerns the staggered ($s = 1$) torus and the 4×5

torus are not bipartite. Their shortest odd loops wind the boundary and have length $L_y + s = 5$ and $L_y = 5$, respectively. Odd moments therefore first enter at order β^5, well beyond the order kept below, and on the bipartite clusters they vanish identically. The second moment counts the allowed directed nearest-neighbor hops: a hop $i \to j$ requires site i occupied and site j empty, which at fixed N_e occurs with probability $N_e(V - N_e)/[V(V-1)]$; with $4V$ directed nearest-neighbor links this gives

$$a_2 \equiv \langle H^2 \rangle_0 = 4t^2 \, \frac{N_e \, (V - N_e)}{V - 1} \quad \xrightarrow{V \to \infty} \quad 4t^2 n(1-n) \, V, \tag{F2}$$

with $n = N_e/V = 1 - x$. From $F = -T \ln Z = -T \ln \Omega_{N_e} - a_2/(2T) + \ldots$ one obtains the leading high-temperature forms, per site,

$$s(T) = s_\infty - \frac{2t^2}{T^2} \, n(1-n), \qquad s_\infty = -n \ln(n/2) - (1-n) \ln(1-n), \tag{F3}$$

$$c_V(T) = \frac{4t^2}{T^2} \, n(1-n), \tag{F4}$$

$$\chi_c^{-1}(T) = \frac{T}{n(1-n)} + \frac{4t^2}{T}. \tag{F5}$$

For comparison with the finite clusters at fixed particle number we use the finite-V expressions, obtained from Eq. (F1) without taking the thermodynamic limit:

$$s = \frac{1}{V} \ln \Omega_{N_e} - \frac{2t^2}{T^2} \, \frac{N_e(V - N_e)}{V(V-1)}, \tag{F6}$$

$$c_V = \frac{4t^2}{T^2} \, \frac{N_e(V - N_e)}{V(V-1)}, \tag{F7}$$

$$\chi_c^{-1} = VT \, \ln\left[\frac{(N_e + 1)(V - N_e + 1)}{N_e \, (V - N_e)} \right] + \frac{4Vt^2}{(V-1) \, T}, \tag{F8}$$

where the first term of Eq. (F8) is obtained by inserting $F_{N_e} = -T \ln \Omega_{N_e}$ into the definition Eq. (B2). These finite-cluster forms are the dashed curves shown in the main text.

For the spin sector, independent spin-1/2 moments give the Curie law with the main-text normalization, $T\chi_s = N_e/(4N) = (1 - x)/4$. In the opposite (Nagaoka) limit the ground-state multiplet has total spin $S_{\rm tot} = N_e/2$; averaging S_z^2 over the degenerate multiplet gives $\langle S_z^2 \rangle = S_{\rm tot}(S_{\rm tot} + 1)/3$, hence

$$T\chi_s \;=\; \frac{N_e(N_e + 2)}{12 \, N}. \tag{F9}$$

The departure of each observable from its high-temperature form defines the crossover scale $T_{\rm quant}$ operationally; as expected for a crossover (rather than a transition), the resulting scale varies somewhat between observables, $T_{\rm quant} \approx 0.5$–$0.8 \, t$.

Appendix G: Nagaoka ferromagnetism and spin stiffness

The lower boundary of the semi-quantum regime is set by the coherence scale $T_{\rm coh}$ associated with the ferromagnetic correlations of the low-doping ground state [33, 34]. Here we estimate the associated spin stiffness for a single hole and recall how it sets $T_{\rm coh} \sim xt$.

For one hole on a cluster of N sites, the ground state is the fully polarized Nagaoka ferromagnet, and the hole occupies the top of the single-particle band at $\mathbf{k}_0 = (\pi, \pi)$: with all $\mathbf{k}$ states but $\mathbf{k}_0$ filled by spin-aligned electrons,

$$E_0 = \sum_{\mathbf{k} \neq \mathbf{k}_0} \epsilon(\mathbf{k}) = -\epsilon(\mathbf{k}_0) = -4t, \qquad \epsilon(\mathbf{k}) = -2t\,(\cos k_x + \cos k_y). \tag{G1}$$

To extract the stiffness of the ferromagnet we impose a uniform spin twist of total angle ϕ across the x direction, i.e., a local spin rotation by $n_x\alpha$ with $\alpha = \phi/L$. The local "up" direction then rotates from site to site, and the overlap of neighboring spinors reduces the effective hopping of the polarized band,

$$t \;\to\; \langle \uparrow_{\mathbf{r}} \,|\, \uparrow_{\mathbf{r}+\hat{x}} \rangle\, t = \cos\!\Big(\frac{\phi}{2L}\Big)\, t, \tag{G2}$$

for x bonds only. Keeping the hole at $\mathbf{k}_0$, the ground-state energy shift is

$$\Delta E(\phi) = 2t \left[1 - \cos\!\Big(\frac{\phi}{2L}\Big)\right] \approx \frac{t\,\phi^2}{4L^2}. \tag{G3}$$

Matching to the continuum stiffness definition in $d = 2$, $\Delta E/L^d = (\rho_s/2)\,(\phi/L)^2$, gives

$$\rho_s = \frac{x\,t}{2}, \qquad x = \frac{1}{N}, \tag{G4}$$

i.e., a stiffness of order xt, carried by the mobile holes. At any finite temperature the two-dimensional ferromagnet is disordered, but with an exponentially growing correlation length,

$$\xi_{\rm FM}(T) \sim \exp\!\left(\frac{2\pi\rho_s}{T}\right), \tag{G5}$$

so that for $T \lesssim T_{\rm coh} \sim xt$ the holes effectively move through an ordered spin background as coherent spinless fermions.

Appendix H: Variational bound for the caging free energy

The caging construction of the main text is controlled by the thermodynamic variational principle. Let $H_{\rm tr}$ be obtained from H by cutting all hopping bonds that cross the boundary of a chosen

cage region, with the hole inside the cage and the exterior half filled. The Gibbs–Bogoliubov inequality, $F \le F_{\rm tr} + \langle H - H_{\rm tr}\rangle_{\rm tr}$, immediately gives $F \le F_{\rm tr}$: $H_{\rm tr}$ conserves the particle numbers of the cage and of the exterior separately, every term of $H - H_{\rm tr}$ transfers a particle across the boundary, and hence $\langle H - H_{\rm tr}\rangle_{\rm tr} = 0$. Moreover, at $U = \infty$ the half-filled exterior has no charge dynamics, so the trial free energy is additive,

$$F_{\rm tr}(N_{\rm cage}, T) = F_{\rm cage}(N_{\rm cage}, T) - (N - N_{\rm cage})\, T \ln 2, \tag{H1}$$

with $F_{\rm cage}$ the free energy of the isolated cage (an open-boundary cluster of $N_{\rm cage}$ sites containing one hole), obtained by exact diagonalization of the cage alone. Throughout this work $\Delta F_{\rm cage} \equiv F_{\rm tr} - F \ge 0$ denotes the caging free-energy cost. At high temperatures it approaches the positional-entropy cost of confining the hole, $\Delta F_{\rm cage} \to T \ln(N/N_{\rm cage})$, which follows from the exact $T \to \infty$ state counts $N\, 2^{N-1}$ and $N_{\rm cage}\, 2^{N-1}$ of the full and trial systems, respectively. We therefore consider the residual cost

$$\Delta\widetilde{F}_{\rm cage}(N_{\rm cage}, T) \;\equiv\; \Delta F_{\rm cage}(N_{\rm cage}, T) - T \ln(N/N_{\rm cage}), \tag{H2}$$

which measures the confinement cost beyond positional entropy. The figures show the dimensionless ratio $\Delta\widetilde{F}_{\rm cage}/T$: it vanishes at high temperature, where the free energy is local; is of order unity through much of the semi-quantum window, so that confinement on the cage scale costs of order the thermal scale; and grows rapidly on cooling toward $T_{\rm coh}$, as discussed in the main text.

1. Cage geometries and effective cage length

Figure 13(a) shows the residual confinement cost of the 2×8 ladder with a single hole ($x = 1/16$), for cages $2 \times n$ with $n = 1, \ldots, 7$. This quasi-one-dimensional geometry complements the two-dimensional 18-site probe of the main text and, admitting a longer series of cage sizes, resolves the cage-size dependence. Its confinement cost behaves as on the 18-site cluster, of order of the thermal scales across the semi-quantum window and rising on cooling toward $T_{\rm coh}$, showing that effective caging, with a comparable cage length, is not an artifact of the specific two-dimensional cluster.

Over the accessible range of cage sizes, the dependence on cage size is approximately exponential,

$$\Delta\widetilde{F}_{\rm cage}(T, \ell) \;=\; A(T)\, e^{-\ell/\xi_{\rm cage}(T)}, \qquad \ell = \begin{cases} \sqrt{N_{\rm cage}} & \text{(2D cages)}, \\ n & \text{($2 \times n$ ladder cages)}, \end{cases} \tag{H3}$$

which defines an effective cage length $\xi_{\rm cage}(T)$ [Fig. 13(b,c,d)]. The fitted length is short and weakly temperature dependent across the semi-quantum window, $\xi_{\rm cage} \approx 1.5$ lattice spacings on

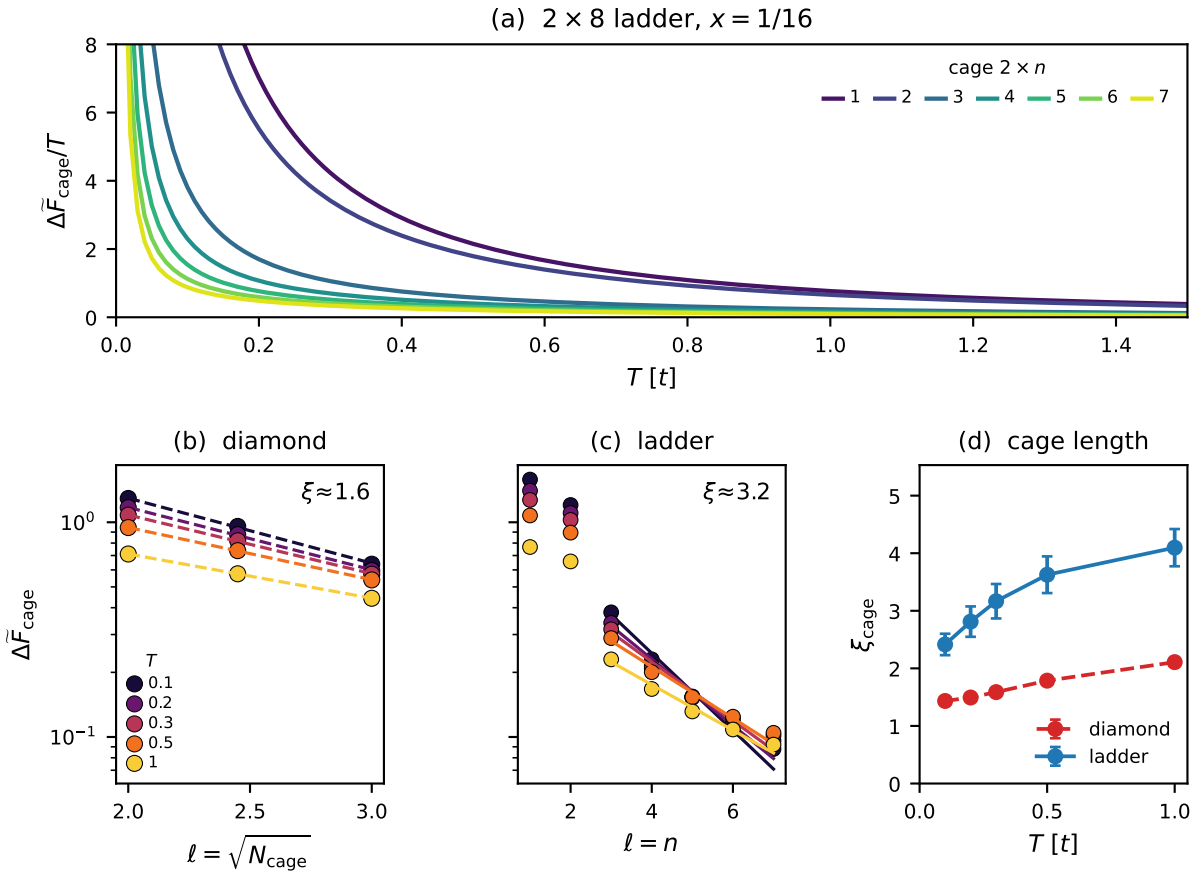


Figure 13. **Cage confinement cost, cage-size scaling, and cage length.** (**a**) Residual confinement cost $\Delta\widetilde{F}_{\rm cage}/T$ [Eq. (H2)] versus temperature for the $2\times n$ cages ($n=1,\ldots,7$) on the 2×8 ladder ($x=1/16$). Bonds crossing the cage boundary are cut; the hole is confined to the cage and the exterior remains half filled. (The corresponding cost for the 18-site diamond is shown in Fig. 5C.) Throughout the semi-quantum window the cost remains order the thermal scale, $\Delta\widetilde{F}_{\rm cage}/T\sim 1$, growing rapidly only on approaching $T_{\rm coh}$. (**b**,**c**) Cage-size dependence of the confinement cost: $\Delta\widetilde{F}_{\rm cage}$ versus cage linear size ℓ on a logarithmic scale, with the exponential fits of Eq. (H3) [$\ell=\sqrt{N_{\rm cage}}$ for the 18-site diamond cages 2×2, 3×2, 3×3; $\ell=n$ for the $2\times n$ ladder cages], at temperatures $T=0.1$–$1.5\,t$. (**d**) Fitted cage length $\xi_{\rm cage}(T)$ for both geometries.

the 18-site cluster and ≈ 2.8 on the ladder. A short, nearly T-independent $\xi_{\rm cage}$ supports the interpretation of charge motion in the semi-quantum regime as quasi-local and controlled by a finite spin environment around the hole rather than by delocalization across the system. On cooling toward $T_{\rm coh}$ the dimensionless confinement cost $\Delta\widetilde{F}_{\rm cage}/T$ rises sharply [Fig. 13(a)], signaling the breakdown of the caging description as ferromagnetic coherence sets in and the hole delocalizes.

Supplementary Files

This is a list of supplementary files associated with this preprint. Click to download.

- hubbardSMnat.pdf